

SPECIFIC FREQUENCIES AND LUMINOSITY PROFILES OF CLUSTER GALAXIES
AND INTRACLUSTER LIGHT IN ABELL 1689

K. A. ALAMO-MARTÍNEZ¹ AND J. P. BLAKESLEE²

¹*Instituto de Astrofísica, Pontificia Universidad Católica de Chile, 7820436 Macul, Santiago, Chile*

²*Herzberg Astronomy & Astrophysics, National Research Council of Canada, Victoria, BC V9E 2E7, Canada*

(Accepted September 24, 2017)

Submitted to ApJ

ABSTRACT

We present magnitudes and profile fits for 180 galaxies in the central field of the massive lensing cluster Abell 1689 using very deep imaging with the *Hubble Space Telescope* Advanced Camera for Surveys in the F814W bandpass. Previous work revealed an exceptionally large number of globular clusters (GCs) in A1689 and mapped their number density distribution. We decompose this number density map into GCs associated with individual cluster galaxies and ICGCs (intracluster globular clusters) associated with the intracluster light (ICL). In all, we measure GC specific frequencies S_N for 33 cluster members and the ICL. The relation between S_N and galaxy magnitude is consistent with the trend observed in Virgo, although some intermediate luminosity galaxies scatter to $S_N > 10$. We estimate the ICL makes up 11% of the starlight in this field, whereas the ICGCs account for $\sim 35\%$ of the GCs, both consistent with predictions from simulations. Galaxies with higher S_N values tend to be rounder, and there is a marginally significant trend of decreasing S_N with increasing specific angular momenta λ_R . We also reevaluate the GC population in the A2744 Frontier Field, for which fewer than one-tenth as many GCs have been detected because of its larger distance. Finally, our core-Sérsic fit to the light profile of the A1689 BCG implies a break radius of 3.8 kpc, among the largest known; we discuss implications of the sizable core and extensive GC population for the supermassive black hole in light of scaling relations.

Keywords: galaxies: clusters: individual (Abell 1689) — galaxies: elliptical and lenticular, cD — galaxies: star clusters: general — globular clusters: general

arXiv:1710.01322v1 [astro-ph.GA] 3 Oct 2017

1. INTRODUCTION

It has been known for the better part of a century that the morphological and spectral properties of galaxies correlate with the surrounding environment (e.g., Spitzer & Baade 1951; Zwicky & Humason 1964; Abell 1965; Einasto et al. 1974; Oemler 1974). In the intervening years, numerous studies have used large observational data sets or numerical simulations to explore and quantify how the baryonic properties of galaxies are molded by their surroundings (e.g., Dressler 1980; Kauffmann et al. 2004; Postman et al. 2005; Tanaka et al. 2005; Baldry et al. 2006; Chung et al. 2009; Vulcani et al. 2012; Jaffee et al. 2016). Interactions among galaxies and with the prevailing group or cluster medium, as well as the cessation of cold gas accretion, play important roles in the evolution of galaxies within dense regions (e.g., van den Bosch et al. 2008; van der Wel et al. 2010; Peng et al. 2010; Muzzin et al. 2012; Mok et al. 2013; Smethurst et al. 2017). However, many studies suggest such “environmental quenching” mechanisms play a secondary role and are mainly applicable to satellite galaxies, while “self quenching” (e.g., via AGN feedback or other internal processes) of individual galaxies, regulated by halo mass, is the main driver in the evolution for central galaxies (e.g., Mandelbaum et al. 2006; Peng et al. 2012; Wetzel et al. 2013; Tal et al. 2014; Bluck et al. 2016). Still others have argued that these two broad varieties of quenching are no longer distinct for massive galaxies within cluster-sized halos (Knobel et al. 2015); moreover, the diverse underlying physical processes vary with redshift (Balogh et al. 2016; Fossati et al. 2017).

Regardless of the precise balance between environmental and mass-regulated quenching, it is clear that large galaxies today are complex systems, assembled over cosmic time through the merging of multiple stellar systems, gas accretion, and in situ star formation, all subjected to a variety of external and internal transformative processes. These processes are accentuated among the most massive galaxies and within the densest environments; therefore, an arguably good place to study them, or at least their end products, are the massive early-type galaxies that populate the centers of rich clusters. Most of these objects have long ago consumed or lost most of their gas and have settled down to passive evolution along the red sequence (see references above), concealing most of the complex processes that shaped their formation. However, a window into the ancient histories of cluster ellipticals is provided by the abundant populations of globular clusters (GCs) that they retain. Compared to the stellar halos of the galaxies themselves, GCs are relatively simple, old, mainly metal-poor systems that occur in large numbers around early-type cluster galaxies (e.g., Harris 1991; Peng et al. 2008). The surviving GCs are very dense stellar systems that were formed at early epochs and have been widely used as tracers of galactic structure (see reviews by West et al. 2004; Brodie & Strader 2006).

The richness of a GC population is parameterized by its specific frequency S_N (Harris & van den Bergh 1981), the number of GCs per unit V -band galaxy luminosity. Among

early-type galaxies, S_N varies with the absolute magnitude of the galaxy M_V following a U-shape trend: it increases with luminosity on the bright side, reaches a minimum at luminosities $\sim L_V^*$, and then increases as luminosity decreases on the faint side, though with a large dispersion (Harris 2001; Peng et al. 2008). The nonlinear behavior of S_N may be understood if the number of GCs (or the mass contained in them) scales with the total halo mass of the host galaxy (Blakeslee et al. 1997; Blakeslee 1999; Kravtsov & Gnedin 2005; Spitler & Forbes 2009; Hudson et al. 2014; Harris et al. 2017), suggesting that S_N scales inversely with the stellar-to-halo mass relation (Moster et al. 2010; Hudson et al. 2015), or the total star formation efficiency. Peng et al. (2008) also found evidence for an environmental effect within Virgo, whereby the majority of dwarf ellipticals in Virgo with high S_N are located within 1 Mpc of the cD galaxy M87. Moreover, Liu et al. (2016) measured $[\alpha/\text{Fe}]$ for 11 of the faintest galaxies used in Peng et al. (2008), finding a tendency for S_N to increase with $[\alpha/\text{Fe}]$. On the other hand, Georgiev et al. (2010) compiled a large sample of S_N for galaxies of varying morphologies in diverse environments and found no significant environmental trends overall.

Another important component of galaxy clusters is the intracluster light (ICL), diffuse stellar material gravitationally bound to the cluster potential rather than individual galaxies, resulting from tidal stripping and relaxation processes (Gallagher & Ostriker 1972). Numerical simulations and observational evidence suggest that the ICL comprises 10%-40% of the optical light in the cluster (Purcell et al. 2007; Rudick et al. 2011; Contini et al. 2014), although it is often challenging to distinguish this material from extended structures of cluster members. In addition to ICL, tidal interactions must also strip GCs from their parent galaxies, producing a population of intracluster GCs (ICGCs) that are bound to the cluster as a whole (White 1987). Based on estimated distances to several GCs found in the Palomar Observatory Sky Survey, van den Bergh (1958) reported the discovery of several intergalactic GCs (the equivalent of ICGCs outside of clusters) in the Local Group. However, these objects are now generally considered distant members of the Galactic GC system, and the existence of truly intergalactic GCs in the Local Group remains in dispute (Mackey et al. 2016).

West et al. (1995) proposed large numbers of ICGCs could be responsible for the high values of S_N found for many brightest cluster galaxies (BCGs); these high- S_N BCGs would have additional GCs associated to them because of their privileged positions within cluster centers. Interestingly, Abell 1185, a cluster in which the central galaxy is offset from the centroid of the X-ray emission, appears to have a significant population of ICGCs located at the X-ray center of the cluster (Jordán et al. 2003; West et al. 2011). Peng et al. (2011) reported a large number of ICGCs in the Coma cluster, comprising $\sim 30\%$ - 45% of the total population in the core, although with high uncertainties due to the low fraction of the covered area. Evidence also exists for a more modest number of ICGCs in the nearby Virgo cluster (Durrell et al. 2014; Ko et al. 2017). As is the case for the ICL, it is

often difficult to distinguish ICGCs from the outer members of the GC systems of individual cluster galaxies. However, sufficient observational evidence now exists to make ICGCs an established feature of galaxy clusters.

In the present work, we explore the luminosity profiles and specific frequencies of early-type galaxies near the center of Abell 1689 (A1689), an extremely massive galaxy cluster with a very high central density of galaxies. This is a follow-up of our previous study of the GC population in A1689 (Alamo-Martínez et al. 2013, hereafter AM13) where the analysis was done for the cluster as whole, not for individual galaxies. In that work we constrained the total population of GCs within a projected radius of 400 kpc of the center of A1689, and found it to be the most populous GC system known. In this follow-up study, we decompose the stellar light and GC populations into components representing individual galaxies, derive S_N values for ~ 30 members, and constrain the ICL and number of ICGCs. The following section summarizes the observational data and reductions. Section 3 describes the modeling of the galaxy profiles, GC populations, and ICL. In Section 4, we present the resulting specific frequencies, explore a possible correlation with kinematics from the literature, examine the possibility of offsets between the galaxy light and GC systems, and discuss a lower mass estimate for the black hole in the A1689 cD galaxy. Section 5 presents our conclusions. For consistency with our AM13 study, we adopt a cosmology with $(h, \Omega_m, \Omega_\lambda) = (0.70, 0.27, 0.73)$, giving a distance modulus for A1689 ($z = 0.183$) of $(m-M) = 39.738$ mag and a physical scale of 3.07 kpc arcsec $^{-1}$. All magnitudes are on the AB system except where noted otherwise.

2. DATA

2.1. Hubble Observation Summary

The current work uses the same deep imaging data, obtained in Program GO-11710 with the *Hubble Space Telescope* (*HST*) Advanced Camera for Surveys Wide Field Channel (ACS/WFC), as was analyzed by AM13. To summarize, we observed the central region of A1689 for 28 orbits in the F814W bandpass, the ACS/WFC bandpass with the highest total throughput. The individual exposures were calibrated with the standard *HST* pipeline, corrected for charge transfer inefficiency (Anderson & Bedin 2010), and then geometrically corrected and combined with the Apsis pipeline (Blakeslee et al. 2003) into a single stacked image of total exposure time 75,172 s and a resampled pixel scale of $0''.033$ pix $^{-1}$. The point spread function (PSF) in the final image has a full width at half maximum (FWHM) of $0''.086$, or 2.6 pix, and thus is adequately sampled. As in AM13, we use the AB photometric system, on which the F814W zero point is 25.947 mag; the Galactic extinction towards A1689 in this bandpass is 0.04 mag (Schlafly & Finkbeiner 2011). We refer the reader to AM13 for a more detailed description of the observations and image reductions.

2.2. Globular cluster density map

At the distance of A1689, the GCs appear as point sources. Thus, in AM13 we optimized the source detection and magnitude measurements for point sources. The source detection was done with SExtractor (Bertin & Arnouts 1996) on a residual image with all large galaxies subtracted, bright stars and areas of poor subtraction masked, and a ring median filter applied; magnitudes were derived from PSF photometry using DAOPhot (Stetson 1987) on an unfiltered version of the residual image at the coordinates of the SExtractor detections. We performed detailed, realistic completeness tests, where the input magnitudes of the artificial stars followed a Gaussian distribution modeled on the expected globular cluster luminosity function (GCLF). The fraction of recovered stars as function of magnitude was described by a four-parameter modified-Fermi function that included the effect of Eddington bias on the magnitudes near the detection limit (see AM13 for details). Furthermore, we corrected for contamination from background galaxies and foreground stars and included the effect of gravitational lensing on the spatial and magnitude distributions of the background galaxies.

In AM13, we detected a total of 8283 unresolved sources (classified as point sources by DAOPhot sharpness and goodness-of-fit criteria) within the ACS/WFC field of view (FOV) over the magnitude range $27.0 < I_{814} < 29.32$ mag, where the faint limit corresponds to the magnitude where we recovered 50% of the sources in the completeness tests, and the bright limit corresponds to $\sim 3\sigma$ brighter than the turnover of the GCLF. (Note that the value of 8212 point source detections quoted by AM13 over this magnitude range referred only to objects within the FOV and inside a projected radius of 400 kpc of the cD galaxy; see Fig. 3 of that work). Using the coordinates of the objects in this sample, we constructed a surface number density map of GC candidates, corrected for incompleteness and background contamination as detailed in AM13, by smoothing with a Gaussian filter of FWHM = $10''$ ($\sigma = 4''.25$). Masked regions were interpolated; following these corrections, the integral of the GC density map over the FOV gives 7940 objects to the detection limit. This represents just over 5% of the GCLF; the correction for integrating over the GCLF is a factor of ~ 19.3 . AM13 mainly used the GC map for illustrative purposes in comparing to the galaxy light, lensing mass, and X-ray surface brightness distributions. In the present work, we use this number density map to model the GC populations of the individual galaxies and ICL component in A1689.

3. ANALYSIS

3.1. Modeling of individual galaxies

A simple way to characterize quantitatively the structure of any galaxy is through parametric fitting of its luminosity profile, and a Sérsic function (Sérsic 1968) is one of the most widely used models for describing diverse types of galaxies. It has the form:

$$I(r) = I_e \exp \left\{ -b_n \left[\left(\frac{r}{R_e} \right)^{1/n} - 1 \right] \right\}, \quad (1)$$

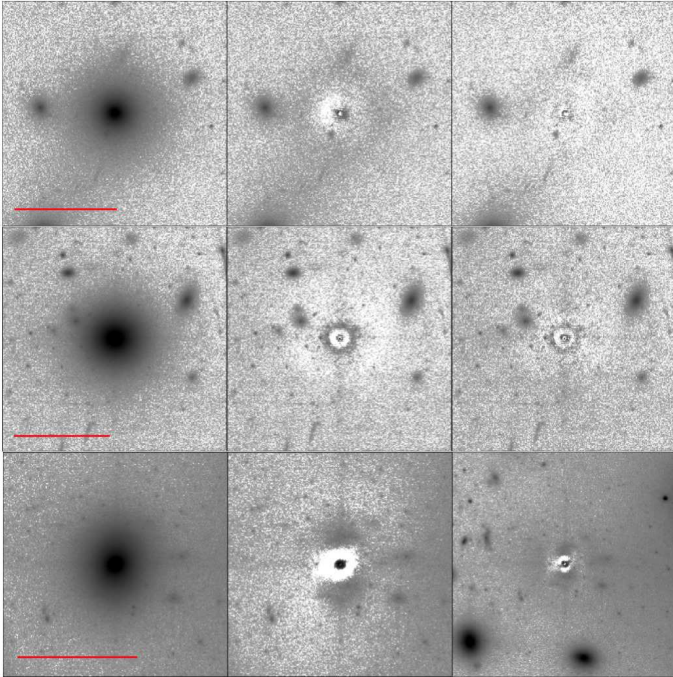


Figure 1. Examples of single versus double Sérsic model fit residuals. Left panels: examples of three typical A1689 galaxies in the ACS/WFC FOV. The red bar indicates the scale corresponding to 5 arcseconds. Middle panels: residuals after subtraction of the best-fit single Sérsic models. Right panels: residuals after subtraction of the best-fit double Sérsic models.

where R_e is the effective radius that encloses half of the light; I_e is the intensity at R_e ; n is the Sérsic index, which governs the shape of the radial profile; and $b_n \approx 1.9992n - 0.3271$ (Graham & Driver 2005). To decompose the contributions of individual galaxies to the total luminosity profile in A1689, we use GALFIT (Peng et al. 2010) to fit 2-D Sérsic functions, convolved with the PSF, to 180 of the brightest galaxies in the ACS/WFC FOV. For selecting the sample of galaxies to be modeled by GALFIT, we used SExtractor with a background grid size `BACK_SIZE=64` pix and `FILTER_SIZE=3`, which we found gave enough leverage to model the background variation without removing much light from the galaxies we wished to detect (the GALFIT modeling was done on the image without this background modeling). The central cD in A1689 is the brightest and most extended galaxy in the cluster, contributing to the local background of many of the other galaxies in the FOV. As a first step in modeling its light distribution, we masked all point and extended sources (except the cD itself) and modeled the galaxy as a single Sérsic profile; this model was then subtracted from the original image. A second iteration of the central galaxy model is done later, after all the other galaxies have been subtracted (see Sec. 3.2).

The sample of 180 galaxies (including the cD) to be fitted was selected based on size and apparent magnitude, without considering cluster membership. By matching these ob-

jects against NED and the sample of A1689 galaxies studied by Halkola et al. (2006; hereafter H06), we found that 94 of the 180 are confirmed (or very likely) cluster members based on spectroscopic or photometric redshifts. For each galaxy in the full sample, a region 20 times larger than the equivalent R_e from SExtractor was extracted, and we used GALFIT to fit simultaneously all the galaxies that fall in the subimage down to 1 mag fainter than the object itself; fainter galaxies and point sources were masked. Due to the very high galactic density in A1689, it is common to have contamination from neighbor galaxies that are close to, but not within, the subimage; thus, we included the sky as a free parameter with an initial guess obtained from a smooth large-scale background map (from a second SExtractor pass with a coarser background grid, `BACK_SIZE=1024`). We used a weight image that included instrumental and photometric contributions, performed the fits with PSF convolution, and constrained the possible range of fitted parameters. We inspected the results of all fits; in some cases, we were able to improve the fit by increasing the subimage size or changing the parameter constraints.

We performed two sets of fits: we modeled each galaxy as both a single and a double component Sérsic profile. At the very deep surface brightness levels reached by our data, complex structure (cores, disks, arms, rings, and tidal features) is discernible in many of the galaxies. Because of the greater flexibility when fitting two Sérsic components instead of one, the results were generally better with the double Sérsic model. Even for apparently smooth and regular ellipticals, the single Sérsic model left notable residuals; some examples are shown in Figure 1. Thus, we opted to use the results from our two-component Sérsic models for all the galaxies. In order to have a single set of parameters characterizing each galaxy, we take the total luminosity to be the sum of the two components and R_e^{GAL} to be the luminosity-weighted average R_e . Using the robust biweight indicator (Beers et al. 1990), the scatter in the differences of the total magnitudes given by the single and double Sérsic fits for all galaxies is 0.20 mag; the scatter estimated from the median absolute deviation ($1.48 \times \text{MAD}$) is 0.16 mag. Dividing these number by $\sqrt{2}$ provides an estimate of the systematic error from the assumed model (probably the dominant uncertainty). We inspected the residuals after subtracting the double Sérsic GALFIT model for each galaxy, and classified the results as reliable (161 galaxies) or unreliable (18 galaxies). In Figure 2, we present histograms of the recovered R_e and n values for our fits; the distributions are fairly typical of those found from Sérsic modeling of other cluster galaxy samples (e.g., Blakeslee et al. 2006; Ferrarese et al. 2006). The fitted photometric parameters are tabulated in Appendix A.

A1689 has been extensively studied because of its extreme mass, high galaxy density, numerous arcs, and relatively modest redshift. One particular study relevant to the present work is that of H06, who analyzed earlier ACS/WFC data and used a combination of strong lensing and masses estimated for individual galaxies to derive the total and stellar mass distributions in the cluster. To estimate the galaxy masses,

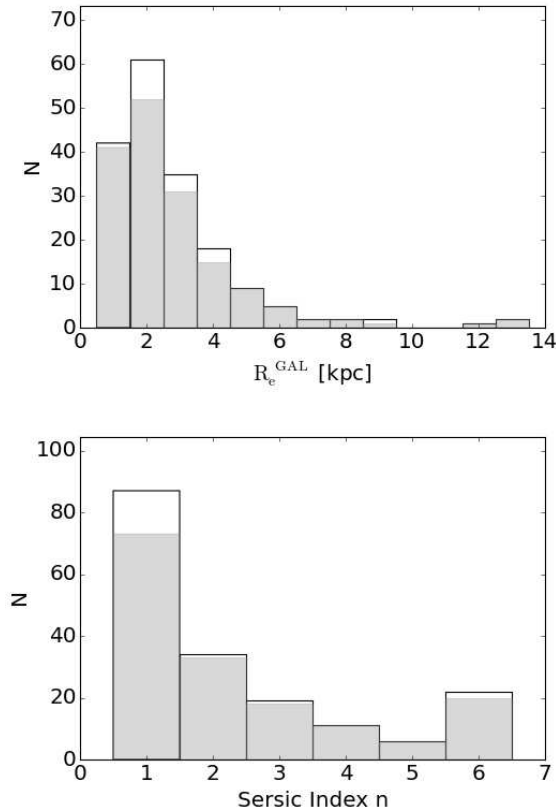


Figure 2. Top: Histogram of R_e^{GAL} values for all 180 galaxies that were modeled in the ACS FOV (open histogram with thick black lines); the filled gray region indicates the R_e^{GAL} values of the 161 galaxies with fits classified as reliable. Bottom: Same as the top panel, but for the Sérsic index n .

they derived structural parameters by fitting Sérsic profiles and assumed the galaxies followed the fundamental plane. The H06 imaging data had only 16% of the exposure time of our deep F814W images and were taken in the F775W bandpass, which is 34% narrower. The signal-to-noise of our photometric data is therefore a factor of 3 greater.

Figure 3 compares our total I_{814} magnitudes to the F775W (i_{775} , similar to SDSS i') magnitudes reported by H06. We have applied a 0.044 mag correction for Galactic extinction (Schlafly & Finkbeiner 2011) to the uncorrected H06 magnitudes, as well as an offset for the expected color ($i_{775} - I_{814}$) = 0.10 ± 0.02 mag, calculated for an early-type galaxy spectrum at $z=0.18$. Of the 80 galaxies they measured, 77 unambiguously match objects in our sample. Of the H06 objects that were not matched, one is outside our field because the observations had slightly different orientations; another is a highly elongated, tangentially aligned object that we masked as a possible background arc; and the third may have a positional error because it is several arcseconds away from an unmatched galaxy that we modeled. In addition, we have used a different approach to fitting the cD (see the following section), so we use a different symbol

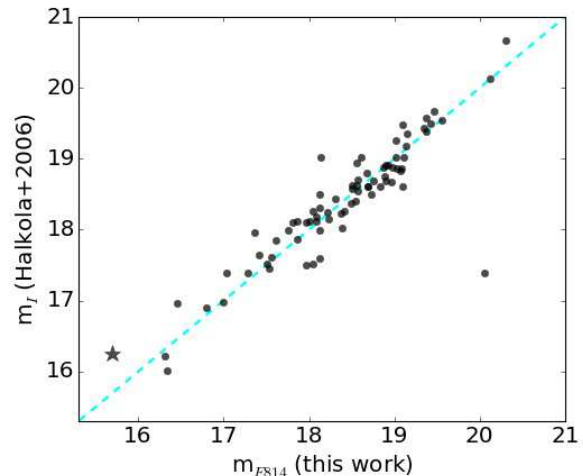


Figure 3. Comparison of the total apparent F814W ($\sim I$) magnitudes measured in this study to the total F775W (\sim SDSS i) magnitudes reported by Halkola et al. (2006). The published F775W magnitudes have been shifted by 0.14 mag to account for both the Galactic extinction and the calculated passband offset for early-type galaxies at $z = 0.18$. The blue dashed line indicates equality. The star represents the cD galaxy which is modeled using a different approach. The galaxy with the large ~ 2.5 mag offset appears to be modeled accurately in our analysis. See text for details.

to represent it (a star). For the matched objects, our magnitude measurements agree very well with H06, except for one very deviant point, which H06 find to be 2.5 mag brighter than we do. The discrepant object is a small galaxy located within a dense region near the cluster center; examining our residuals, we are confident our measurement is accurate. It is likely that the H06 model for this one galaxy was contaminated by light from its brighter neighbors, especially the cD, but again we emphasize the overall agreement. The median offset (after the above extinction and color corrections) is 0.02 mag, and the biweight scatter in the differences is 0.24 mag, or 0.22 mag if estimated from the MAD. Assuming that the two data sets contribute equally to the scatter and dividing by $\sqrt{2}$ implies a measurement error of ~ 0.15 mag. Given the higher signal-to-noise of our images, this seems a conservative estimate of the errors.

3.2. Modeling the cD and ICL

BCGs occupy the nexus between large-scale structures of $\gtrsim 1$ Mpc, and the \sim kpc scales of individual galaxies. Their structures are intricately intertwined with that of the surrounding cluster, including the ICL, making it a challenge to disentangle properties such as total stellar luminosity or the size of the GC population. The cD galaxies were first identified on photographic plates and defined by Matthews et al. (1964) as elliptical BCGs located in the centers of galaxy clusters and surrounded by extended low surface brightness envelopes (many were also associated with

radio sources). In A1689, the BCG has an extended, low surface brightness profile and thus is classified as a cD; we refer to it interchangeably by either term. However, the definition of cD has actually become less clear with the advance of astronomical instrumentation. The supposed unique characteristic of cD galaxies is the extended envelope, originally characterized as an excess at large radii with respect to a de Vaucouleurs profile (Sérsic with $n = 4$), but such a profile might also be represented by a Sérsic of higher n . In the literature, cD profiles have been modeled as: a double de Vaucouleurs profile, de Vaucouleurs + exponential, Sérsic + exponential, and a single Sérsic with $n > 6$ (Gonzalez et al. 2005; Seigar et al. 2007; Donzelli et al. 2011; Bender et al. 2015). Despite the diverse representations, there is a general consensus that a significant portion of the extended envelope results from stripping of cluster galaxies (Gallagher & Ostriker 1972; Vílchez-Gómez 1999; Gonzalez et al. 2005). Stellar material stripped from cluster galaxies is also one definition of the ICL; thus, in some cases, the difference between a cD envelope and ICL may be a matter of semantics.

Kinematic information can provide insight into the transition from BCG to extended halo or ICL, especially if there is an offset between the velocities of the BCG and cluster. Based on mean velocity and dispersion, Bender et al. (2015) showed that the envelope of the cD NGC 6166 does not belong dynamically to the central galaxy but to the surrounding A2199 cluster potential. Interestingly, although they were able to measure distinct kinematics for the galaxy and the envelope (or ICL), they did not find any photometric discontinuity between these components, and the overall surface brightness profile was well fitted with a single Sérsic model. More generally, Veale et al. (2017b) analyzed the wide-field kinematics of a complete mass-selected sample of luminous early-type galaxies and found that those in cluster-sized halos preferentially show rising dispersion profiles at large radius, while equally massive galaxies with similar profiles, but in more isolated regions, generally show radially declining dispersions. Thus, disentangling a BCG halo from ICL may require both photometric and kinematical profiles. However, this becomes difficult at large distances and in very dense regions with numerous overlapping galaxies, such as in A1689.

In order to model accurately the extended profile of the central galaxy and extended light, we subtracted the models for the other 179 galaxies that we had fitted, masked other bright objects and areas of poor residuals, and used the task *ellipse* within IRAF to measure the isophotes of the remaining light. Because the galaxy is not circular but elliptical, we calculate the equivalent circularized radius as $R^{circ} = a\sqrt{1 - \epsilon}$ where a is the semi-major axis and ϵ is the ellipticity of the isophote. In Figure 4, the black points show the radial surface brightness profile of the central component, which includes the light from the BCG and an obvious extra component at large radii that we attribute to ICL.

The radial surface brightness profiles of the most massive elliptical galaxies generally flatten at small radii, so that their central surface brightness is lower than the inward extrapolation of the best-fit outer Sérsic model. Such pro-

files can be well described by a “core-Sérsic” model (Graham et al. 2003; Trujillo et al. 2004), a Sérsic profile that flattens to an inner power-law; it has the following form:

$$I(r) = I_b 2^{-(\gamma/\alpha)} \exp \left[b_n \left(2^{1/\alpha} \frac{R_b}{R_e} \right)^{1/n} \right] \times \left[1 + \left(\frac{R_b}{r} \right)^\alpha \right]^{\gamma/\alpha} \exp \left\{ -b_n \left[\frac{R^\alpha + R_b^\alpha}{R_e^\alpha} \right]^{1/(\alpha n)} \right\}, \quad (2)$$

where R_b is the break radius (transition point between a standard Sérsic profile and the inner power-law), I_b is the intensity at R_b , α indicates how sharp the transition is, and γ is the slope of the inner component.

We tried multiple approaches for simultaneously fitting the central galaxy and ICL with a combination of core-Sérsic and Sérsic functions, using a maximum likelihood method. First, we performed the analysis with all the parameters free; the resulting fit is shown in the top panel of Figure 4. The fit appears excellent and gives a combined integrated magnitude of $m_{814} = 14.7$ mag; the central core-Sérsic model, representing the BCG, contributes only $\sim 18\%$ of the light in this model, and the remaining $\sim 82\%$ is ICL. However, the best-fit $n = 1.4$ for the BCG is lower than expected for such a bright galaxy, while the ICL component has $n=2$.

Donzelli et al. (2011) analyzed the surface brightness profiles of 430 BCGs, finding that half of the sample required two Sérsic components: an inner one with $1 \lesssim n \lesssim 7$, plus an outer exponential ($n \approx 1$) component. Thus, it is somewhat unusual for the ICL component to have a larger Sérsic index than the BCG. Moreover, core-Sérsic galaxies generally have $n > 4$, even when they are not BCGs. For instance, the galaxy sample analyzed by Kormendy et al. (2009) included 10 classed as “core galaxies,” which had best-fit Sérsic indices ranging from 5.2 to 11.8. The largest n was for M87, which might be “biased” by an ICL component. However, with M87 excluded, the remaining 9 core galaxies had a median n of 7.1, with no significant correlation with luminosity (all the cored galaxies were luminous). This is consistent with the results of Ferrarese et al. (2006), who fitted multi-band profiles to 100 galaxies in the Virgo cluster, including core-Sérsic models for the brightest ones. Thus, $n \approx 7$ appears to be a good average for galaxies that are well described by core-Sérsic models.

We therefore performed another fit to the combined BCG + ICL profile in A1689, constraining $n = 7$ for the core-Sérsic component; the rest of the parameters were left free. The result is shown in the middle panel of Figure 4. The combined magnitude is again $m_{814} = 14.7$ mag (the total luminosity is well constrained), but in this case, the contribution from the BCG is 41%, more than double the amount when all parameters were free. For the ICL component, we find $n = 1.6$, which is very similar to the results of Cooper et al. (2015), who fitted double Sérsic profiles to high-resolution N-body simulations of galaxy clusters and

found a median best-fit value of $n = 1.66$ for the diffuse outer component.

In order to explore the maximum amount of light that could be assigned to the BCG, we tried a third case in which we only fitted a single core-Sérsic model to the light within $R^{\text{circ}} < 25$ kpc, and then took the integral of this fit as the total BCG luminosity. The result is shown in the bottom panel of Figure 4. In this case, the BCG has $n = 8.7$, which is still within the observed range, with magnitude $m_{814} = 15.0$ mag; since the total magnitude of the combined distribution is 14.7 mag, the BCG represents $\sim 77\%$ of the light in this case, and the ICL (representing the excess of light with respect to the single model) would have an integrated $m_{814} = 16.3$ mag. This is a lower limit on the ICL, which must contribute at least some luminosity even at projected radii < 25 kpc. Overall, we prefer the second model, with n constrained for the core-Sérsic component based on literature considerations, the BCG contributing $\sim 40\%$ of the light, and the ICL accounting for the remaining $\sim 60\%$. We use this model in the following sections to estimate separately the specific frequencies of the BCG and ICL. However, it should be remembered that the plausible range for the ICL component is anywhere from $\sim 23\%$ to $\sim 82\%$.

Figure 5 (middle panel) shows our final 2-D galaxy light model, constructed from the GALFIT models of the 179 non-central galaxies and our *ellipse* model for the combined cD and ICL. The left panel of Figure 5 shows the ACS/WFC image, and the right panel shows the residuals after subtracting the full luminosity model. Although only 94 of the modeled galaxies are confirmed members of A1689, the models for the other galaxies are needed to characterize the full light distribution and derive accurate magnitudes for the known members. Note that areas of imperfect galaxy subtraction were masked before deriving the isophotal model described above; thus, the excess of light associated with the clump of galaxies to the upper right of the cD did not contribute to the ICL component seen in the 1-D profiles of Figure 4.

3.3. Modeling of globular cluster systems

The situation for the GC spatial distribution is similar to the case of the starlight in the sense that the GC populations of many galaxies in the FOV overlap. We therefore follow a similar approach: we use the 2-D GC number density map (described in Sec. 2.2 above) and simultaneously fit multiple Sérsic components to it with GALFIT. However, we were not able to identify a significant GC system (an excess of point sources on the map) for many of the galaxies modeled previously from the starlight. The main reason for this is that, as shown by AM13, the GCs only represent $\sim 0.8\%$ of the stellar mass in the field, and thus have a much lower signal-to-noise ratio than the starlight. In addition, the Gaussian filtering, which was necessary to have a continuous number density map, smooths out the overdensities for many of the smaller galaxies. The filtering was done on a physical scale of $\sigma = 13$ kpc, so only galaxies that have significant excesses on this scale can be modeled.

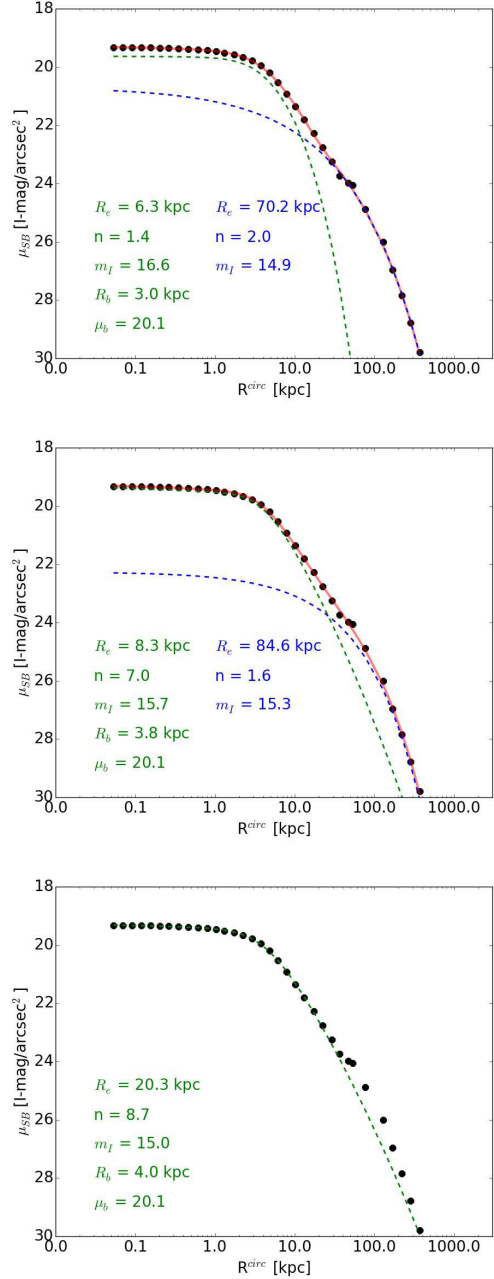


Figure 4. F814W surface brightness radial profile (black dots) after subtracting 179 modeled galaxies in the field and masking all other sources except the BCG and ICL. In all panels, the surface brightness of each isophote is plotted as a function of the isophote’s circularized radius. In the top two panels, the green dashed curve shows the best core-Sérsic fit (representing the BCG), the blue dashed curve shows the best Sérsic fit (representing the ICL), and the red curve is the sum of the two. The bottom panel shows the result for a single core-Sérsic model, fitted only to the isophotes with $R^{\text{circ}} < 25$ kpc. The fit parameters are shown in each panel. The preferred decomposition model is the one in the middle panel with the $n = 7$ for the BCG; see text for details.

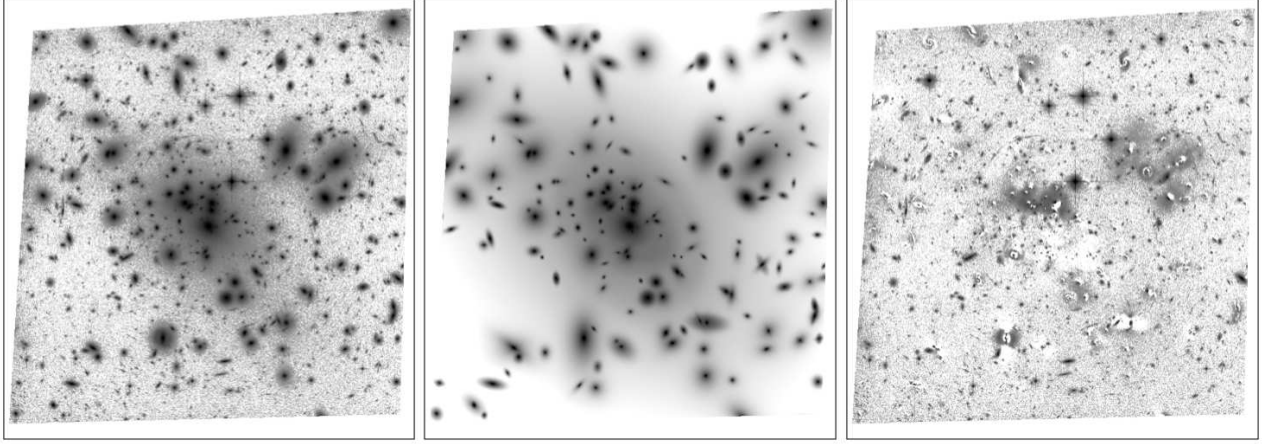


Figure 5. Left: the deep ACS/WFC F814W image of the galaxy cluster A1689 (FOV $\sim 3'3 \times 3'3$), reduced as detailed in AM13. Middle: our final luminosity model, representing the light profiles of 180 galaxies and the ICL in A1689. Right: the image residuals after subtracting the final model from the original image. (The residuals associated with the group of galaxies to the upper right of center were masked when fitting the combined light of the cD + ICL.)

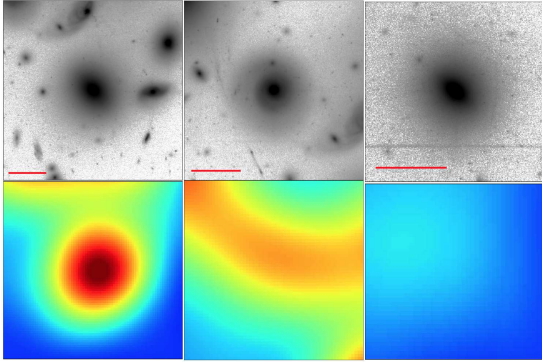


Figure 6. Three examples of cases where both the galaxy and GC system were modeled. Top: typical modeled galaxies in the ACS field. The red bar indicates the scale corresponding to 5 arcseconds. Bottom: the corresponding regions in the GC number density map. The GC system of the galaxy shown in the top middle panel blends in with those of neighboring galaxies on either side, producing the arc-like distribution seen in the bottom middle panel. However, these galaxies were simultaneously modeled in order to decompose their overlapping GC systems into separate components.

To select the GC systems to be fitted, we visually inspected the subimage region of the GC number density map corresponding to each of the 180 galaxies (including the cD) for which we had modeled the stellar light with GALFIT. We selected the cases where a significant excess was identifiable (see Figure 6 for some examples), resulting in a sample of 66 GC systems to be fitted. Because of the extensive overlapping of GC systems on the smoothed map, rather than analyzing small subimages around each galaxy, we divided the GC map into quadrants (see Figure 7). Within each quadrant, we performed simultaneous fitting of all the selected GC systems within it, as well as an extended background component for the central GC system. Each GC system was modeled by a single Sérsic function convolved with the smoothing ker-

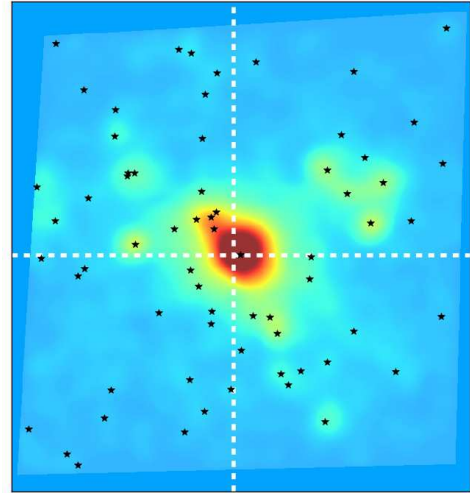


Figure 7. Smoothed globular cluster surface number density map, corrected for background, incompleteness, and masked areas. The black stars show the central locations of the host galaxy light for the 66 GC systems (including BCG) that were modeled. The dashed white lines indicate the quadrants used for the multiple fitting.

nel used in constructing the map. The initial guesses for the Sérsic parameters were taken to be the best-fit values from the galaxy models in Sec. 3.1. The effective radius of each GC system R_e^{GC} was constrained to be between 0.5 and 4.0 times R_e^{GAL} (e.g., Peng et al. 2008), the central coordinates were constrained to be no more than 3 kpc in X and Y from the galaxy center (giving a maximum offset of 4.2 kpc, which is large but only $\sim 1/3$ of the smoothing kernel), and a minimum normalization of 50 GCs was imposed. Because the GC system of the cD galaxy overlaps all of the quadrants, it was modeled again, independently, using the full map after subtracting all other models, as detailed below.

We inspected all 66 GC models and their residuals after subtraction from the density map, and visually classified 50 of them as reliable fits. Some examples of the 16 rejected fits are shown in Figure 8. Of the 50 reliable fits, 36 are associated with confirmed cluster members, but in three of these cases, the luminosity model was classified as poor, leaving a sample of 33 confirmed members with good fits for both the GCs and galaxy light. The ratio of the normalizations of these fits yields the GC specific frequencies presented in Sec. 4.2 and tabulated in Appendix A.

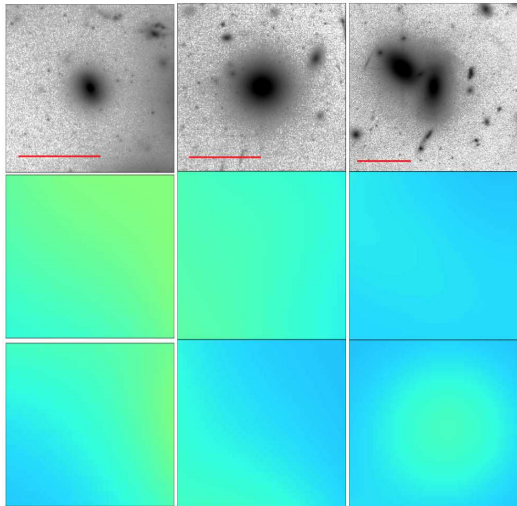


Figure 8. Examples of “bad” GC system models, rejected on the basis of visual inspection. Of the 66 GC systems modeled, 16 were labeled as bad fits, without considering cluster membership criteria. Top row: galaxies; middle row: corresponding locations on the GC density map; bottom row: rejected GC density model. The red bar indicates the scale corresponding to 5 arcseconds.

3.4. Modeling the cD and Intracluster GCs

For the sake of consistency, we wish to follow a similar treatment for the GCs as for the stellar light. Therefore, we again use the *ellipse* task to construct the radial profile of the surface number density of GCs for the central components (black squares in Figure 9, after subtracting Sérsic models for all the other GC systems). We note that Durrell et al. (2014) and Cho et al. (2016) followed a similar approach in modeling the smoothed GC number density maps around the cD galaxies in Virgo and Coma, respectively.

Although an excess in the outer region is not as obvious for the GCs as for the galaxy light, we again perform three types of fits, illustrated in Figure 9: a single core-Sérsic (top panel), a core-Sérsic plus Sérsic (middle panel) and a double Sérsic (i.e., testing the significance of a flat core in the GC distribution; bottom panel). We find that the fit with two standard Sérsic models is significantly worse than the core-Sérsic + Sérsic case; a core of $R_b \approx 20$ kpc is required. Somewhat surprisingly, the model prefers exponential profiles (we constrained $n \geq 1$ for both components), whether or not there

is a core. For consistency with the light, we take the two-component Sérsic/core-Sérsic model, in which $\sim 42\%$ of the GCs are associated with the cD, and the other $\sim 58\%$ are ICGCs. This is remarkably consistent with the decomposition found in Sec. 3.2 for the central galaxy and surrounding ICL, suggesting that the cD and ICL have very similar specific frequencies. However, given the similarity of the fits in the top and middle panels of Figure 9, the uncertainty in the decomposition is large, and a single component model with $n \approx 4$ provides a reasonable fit. It is simply easier to separate the cD from the ICL using the starlight than the GCs, because the surface density of the GCs is so much lower. Figure 10 shows our final GC number density model (middle panel) compared to the observed distribution (left panel). The residuals (right panel) are clearly not perfect, but the model gives a reasonable representation of the gross structure.

4. RESULTS AND DISCUSSION

Of the 180 galaxy profiles and the 66 GC populations modeled in the FOV, 33 galaxies are confirmed A1689 members and have fits classified as reliable for both the galaxy light and GCs. These 33, plus the intracluster components, are discussed in the current section.

4.1. ICL and ICGCs

Although the ICL constitutes a significant amount of the total optical light, it is difficult to detect because of its very diffuse and extended nature. Also, the ICL is centrally concentrated in the cluster, and therefore it is difficult to distinguish from the stellar light of the central galaxy (see Sec. 3.2). There is also evidence that the ICL evolves with time in amount and morphology. This was noted by Schombert (1988), who found that the luminosity of the cD envelope correlates with parameters indicative of the dynamical stage of the cluster, such as richness, morphological type, and X-ray luminosity. Rudick et al. (2006) studied the formation and evolution of ICL in three simulated galaxy clusters, finding that as the galaxy cluster evolves, high luminosity features dilute into fainter and more extended structures. These authors defined the ICL as all the light at V -band surface brightness $\mu_V < 26.5$ mag arcsec $^{-2}$, but a later study (Rudick et al. 2011) found that the amount of ICL increased with time regardless of definition, although the inferred total could vary at any given time by a factor of two, depending on one’s definition.

In Sec. 3.2, we found that the ICL represented $59^{+22}_{-37}\%$ of the combined light of the BCG + ICL in A1689, where the substantial error bars represent the range of values from the different types of compositions we explored. This amounts to $11^{+4}_{-7}\%$ of the total light in the ACS FOV. This is very similar the 7%-15% range found by Mihos et al. (2017) for the Virgo cluster, and consistent with the 10%-40% range found in simulations by Contini et al. (2014), who also noted there was a large halo-to-halo scatter in the ICL fraction, and no clear dependence on halo mass.

We note again that the excess in the surface brightness profile that we modeled as the ICL (Figure 4) was not caused by

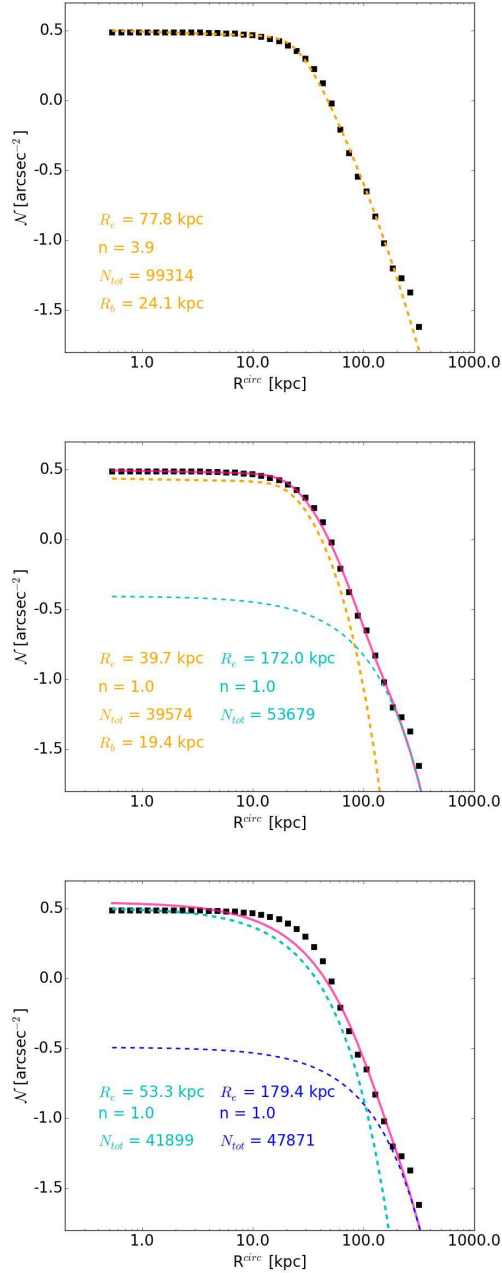


Figure 9. Radial profile of the surface number density of GCs (black squares) after subtracting the 65 GC system models produced by Galfit and masking regions of poor residuals. The orange dashed curve shows the best core-Sérsic fit (representing the GC population of the BCG), the cyan dashed curve shows the best Sérsic fit (representing the ICGCs), and the magenta curve is the sum of the two components. The decomposition shown in the middle panel is our preferred model, which has 42% of the GCs assigned to the BCG component and the rest being associated with the ICL.

the group of galaxies to the upper right of the BCG, since we masked that region when we determined the isophotes. However, as discussed by Mihos et al. (2005, 2017), modeling the ICL with a simple radial profile can be misleading, since it often shows streams and other structures that may be associated with (but not bound to) individual cluster galaxies. Thus, although we believe we have made the best possible decomposition of A1689’s central light profile into BCG and ICL components, the amount of ICL may be underestimated (by ~ 10 -20%), as excess light is visible in the residual image near the locations of some bright galaxies, and this would not be represented within the two-component Sérsic model.

Similarly, although ICGCs appear to be a common feature of galaxy clusters, it is not easy to identify them. The ICGCs blend in with the GC population of the BCG at small cluster-centric radii and have low surface densities blending in with the background at larger radii. As noted above, the only clear detections of ICGCs have been in relatively nearby clusters. However, numerical simulations predict that at least 30% of the total GC populations in evolved clusters may be ICGCs (Yahagi & Bekki 2005), and this is also the fraction of ICGCs found by Peng et al. (2011) for the Coma cluster.

For A1689, we have found in Sec. 3.4 that ICGCs account for about $\sim 58\%$ of the combined BCG + intracluster GC population. This is similar to the breakdown found for the stellar light (and even more uncertain). However, because the S_N of the central component is several times larger than average, the ICGCs represent roughly 35% of the total GC population in the ACS FOV. AM13 did not perform any decompositions, and thus could not estimate a reliable ICGC fraction, but concluded that it was no more than half; our result here is consistent with this upper limit. In this model, the BCG contributes 26% of the GCs to the total, and all the other galaxies in the field contribute the remaining 39%.

4.2. Specific frequencies

The specific frequency is defined as the number of GCs normalized to a galaxy luminosity of $M_V = -15$ (Harris & van den Bergh 1981):

$$S_N = N_{GC} 10^{0.4(M_V+15)}. \quad (3)$$

Early studies showed S_N is dependent on morphological type (Harris 1991). Since then, S_N has been extensively studied in galaxies with different luminosities, morphologies, and environments, in order to understand why N_{GC} does not scale in a simple linear way with the field stars, i.e., why the formation efficiency of GCs per unit stellar mass varies among galaxies. This is an important key for unlocking the early stages of galaxy formation and assembly. It is still not entirely clear what drives the large scatter in S_N for galaxies of the same mass. An important motivation of the current work is to examine the behavior of S_N within the extremely dense environment of the A1689 core and to compare with galaxies that have evolved under different conditions. The total mass of A1689 within 2 Mpc is $1.3 \times 10^{15} M_\odot$ (Serenio et al. 2013). A particularly good comparison sample comes from the 100

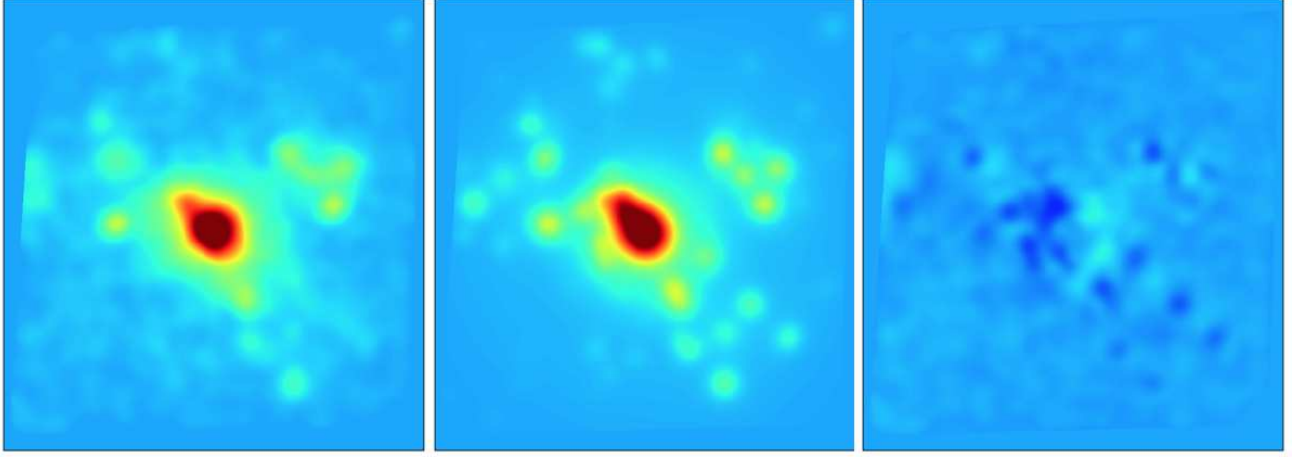


Figure 10. Left: GC surface number density map (as in Fig. 7). Middle: combined models for the GC systems of individual galaxies and the ICGC component. Right: residual after subtraction of the model.

early-type galaxies studied in the ACS Virgo Cluster Survey (ACSVCS; Côté et al. 2004), the largest sample of GC populations analyzed in a homogeneous way. Virgo has a total mass of $5.5 \times 10^{14} M_{\odot}$ (Durrell et al. 2014). As part of the ACSVCS, Peng et al. (2008) confirmed the U-shape trend of S_N with luminosity, and found that most dwarf galaxies with high S_N are located within 1 Mpc of the M87, the central galaxy in Virgo, suggesting an environmental dependence of GC formation efficiency with density. However, the innermost few dwarfs have lower S_N values, probably as a consequence of their GCs being stripped by the strong gravitational tides of M87 or by the cluster itself (and becoming ICGCs).

As in AM13, to estimate the S_N of our A1689 sample, we convert the I-band total magnitudes (corrected for extinction) from GALFIT to V-band using:

$$M_V = M_{814} - K_{814} + (V - I_{814}), \quad (4)$$

where K_{814} is the F814W K-correction of 0.11 mag for a giant elliptical at the redshift of A1689, and $(V - I_{814}) = 0.83$ mag is the rest-frame color on the AB system. Figure 11 shows S_N as function of M_V for the ACSVCS sample (gray dots) and our A1689 sample. The color code of the A1689 points indicates the clustercentric distance. The star and triangle indicate the values for the cD galaxy ($S_N^{\text{cD}} \approx 18$) and the ICL ($S_N^{\text{ICL}} \approx 17$), respectively. The error bars cover the range in magnitudes from the different cases considered in Sec. 3.2.

The orange dashed line indicates S_N as function of galaxy magnitude for a population of 50 GCs, the lower limit imposed in the GALFIT fitting; only a few systems had results actually constrained by this limit. The cyan dashed curves are theoretical predictions from Georgiev et al. (2010), which assume a constant GC formation efficiency $\eta = M_{\text{GC}}/M_h$ per total halo mass M_h , where M_{GC} is the total mass in GCs. The galaxy luminosity for these models is calculated from $L \propto M_h^{5/3}$ for galaxies of stellar mass $M_{\star} < 3 \times 10^{10} M_{\odot}$ (star formation presumed regulated by stellar feedback), and $L \propto M_h^{1/2}$ for galaxies with $M_{\star} > 3 \times 10^{10} M_{\odot}$ (star forma-

tion presumed regulated by virial shocks, including AGN-induced). These simple scalings give a reasonable approximation to the variation in M_h/L with stellar mass. For A1689, we find that most of the galaxies, including the BCG, fall within the range of values observed for systems in the local universe, indicating $1 \times 10^{-5} < \eta < 3.5 \times 10^{-4}$, although the scatter is large and we do not probe a large range in luminosity. As evident from the point colorings, there is a weak tendency for galaxies with higher S_N to be within ~ 150 kpc of the cluster center.

The most outlying point in Figure 11 is located at $M_V \approx -20.5$ and $S_N \approx 14$ and has ID #156 in the data tables. This galaxy is discordant with previous results indicating that galaxies of intermediate luminosity have universally low $S_N \lesssim 2$ (Peng et al. 2008). To examine this object in more detail, the top set of 6 panels in Figure 12 shows a zoomed region around this galaxy, its corresponding location in the GC density map, the galaxy and GC models, and residuals. Interestingly, the galaxy is ~ 250 kpc from the cluster center, outside the heavily crowded region. There is no indication that the fits are poor or misleading in this case, although the GC surface density is fairly low. The galaxy appears quite normal except for its relatively high S_N . Figure 12 also shows the corresponding sets of images for the other two outliers in Figure 11: galaxy #63 (middle set of panels), which has $M_V \approx -21.5$ and $S_N \approx 13$; and galaxy #134 (bottom panels), which has $M_V \approx -21.0$ and $S_N \approx 10$. Only for the third object does it appear that there could be significant contamination from a neighbor galaxy.

4.3. Galaxy kinematics vs. S_N

Despite some broad morphological themes, the early-type galaxy class is comprised of galaxies with a wide range of properties (kinematics, stellar and dust content, mass-to-light ratio, among others). Emsellem et al. (2007, 2011) introduced a kinematical classification for early-type galaxies (accounting for projection effects) by defining two kinematical classes: slow rotators (complex velocity fields with lit-

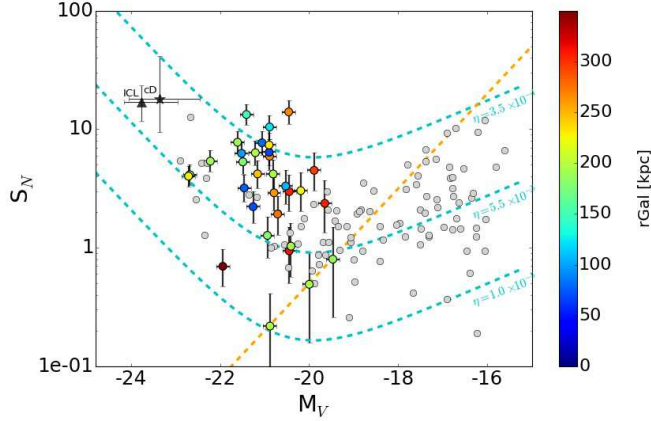


Figure 11. S_N as function of M_V for galaxies in A1689 (colored dots, with color code indicating clustercentric distance according to scale at right) compared to same data for 100 galaxies from the ACS Virgo Cluster Survey (gray dots; from Peng et al. 2008). The A1689 cD is represented by the labeled star, and an estimate of the intracluster S_N is also shown. The cyan curves are predictions from Georgiev et al. (2010) assuming fixed GC formation efficiency η per total halo mass M_h (see explanation in text); the values of η are labeled. The orange dashed line indicates the lower limit of 50 GCs imposed for the A1689 GC system fits.

the net angular momentum, often showing decoupled cores) and fast rotators (ordered velocity fields dominated by rotation). In this classification scheme, only $\sim 30\%$ of morphologically identified early-type galaxies are slow rotators, once considered a common characteristic of spheroidal systems (Cappellari et al. 2011). However, the fraction of slow rotators increases with mass, reaching $\gtrsim 80\%$ for stellar masses $M_\star > 5 \times 10^{11} M_\odot$ (Veale et al. 2017a).

The kinematical classification is based on the projected stellar angular momentum λ_R (measured within R_e) and projected ellipticity ϵ . The boundary between slow and fast rotators is $\lambda_R = 0.31\sqrt{\epsilon}$ (dashed line in bottom panel of Figure 13), with the former being below the line and the latter above. This ‘dichotomy’ is reminiscent of the one pointed out by Bender et al. (1989), who classified elliptical galaxies as boxy or disky based on the deviations of their isophotes from perfect ellipses, and reported correlations of these characteristics with radio and X-ray emission. Numerical simulations (Naab et al. 2009; Lagos et al. 2011; Rodriguez-Gomez et al. 2016) imply that dry major mergers (mass ratios of order 3:1) form boxier, slow-rotating spheroidal systems, while wet or dry minor mergers with high angular momentum results in disky systems. However there is not a sharp demarcation between either the isophotal or kinematical classes, and there appears to be a range of formation scenarios for each case.

Cappellari et al. (2011) studied the kinematical version of the morphology-density and found that as the galactic density increases, the fraction of early-type fast rotators decreases in a manner similar to the decrease of spiral galaxies in

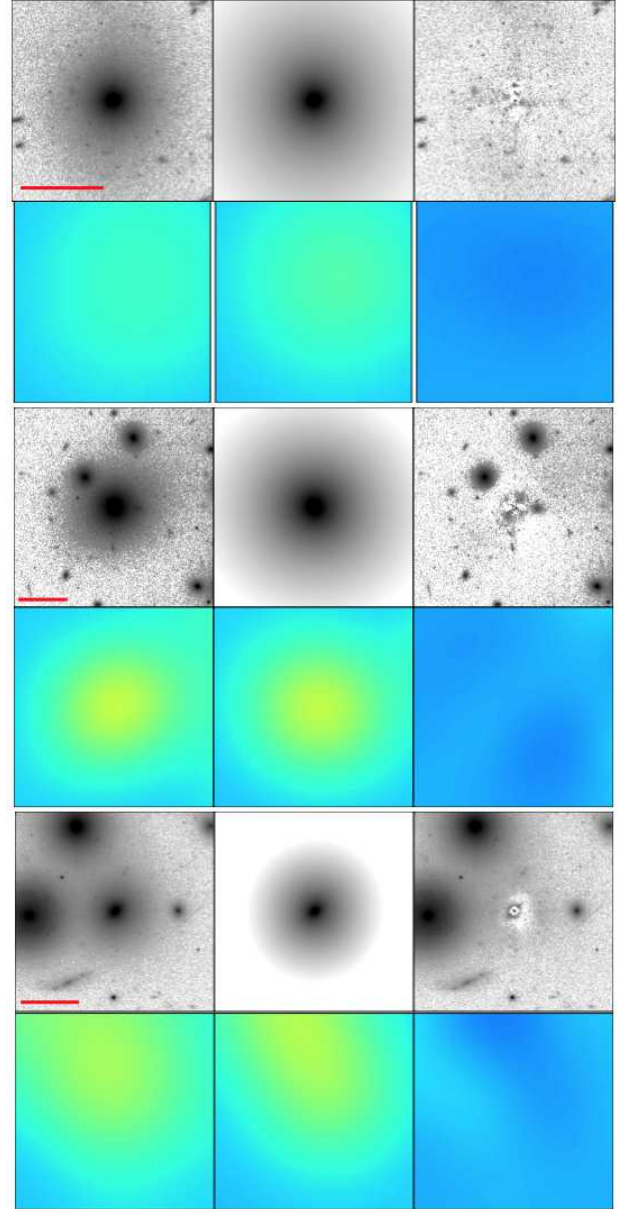


Figure 12. Three intermediate luminosity galaxies with high S_N values; these three objects are the biggest outliers with respect to the blue dashed lines in Figure 11. Each set of six postage stamp panels shows: galaxy image, galaxy model, galaxy residual, GC number density map of same region; GC number density model; GC density residual. The red bar indicates the scale corresponding to 5 arcseconds. The galaxies are ordered from top to bottom by their S_N . The top six panels are for galaxy #156 with $S_N \approx 14$; the middle six are for #63 with $S_N \approx 13$; the bottom six are for #134 with $S_N \approx 10$ (the galaxy and GC fit data are listed in Tables 1 and 2, respectively). For the top two galaxies, the S_N values appear genuinely high, without obvious contamination. For the galaxy at bottom, the GC density distribution blends in with that of the bright galaxy to the upper left; although both galaxies are included in the model, the decomposition may not be perfect. The apparently bright galaxy near the left edge of the bottom panels is actually a lower luminosity foreground spiral without detectable GCs.

the classic morphological version of the relation (Dressler 1980). More specifically, the fraction of slow rotators in their sample was only a few percent, except in the Virgo cluster core, where it increased to $\sim 20\%$. These authors suggested that the dynamical processes operating in high-density environments makes them more efficient in producing slow rotators. More recently, Veale et al. (2017a) explored a wider range of environments and concluded that the apparent trend was actually driven by the underlying correlation of slow rotator fraction with stellar mass, coupled with the tendency for more massive galaxies to occur in higher density regions. Motivated by these considerations, D’Eugenio et al. (2013) determined the fraction of slow rotators in the core of A1689, a much denser environment than the Virgo cluster or any other nearby region. These authors used FLAMES/GIRAFFE on VLT to obtain integral field spectroscopy of 29 bright galaxies in A1689 and measure λ_R , finding a similar fraction of slow rotators as in Virgo, despite the much higher density.

Using these kinematical data, we have made a first attempt to explore the behavior of S_N as a function of λ_R . In the top panel of Figure 13 we reproduce Fig. 4 of D’Eugenio et al. (2013), but only for galaxies for which we were able to estimate S_N , with the S_N values indicated by the color code. Given the sample size, it is difficult to make general conclusions, but it is clear that the slow rotators do not all have high S_N values. On the other hand, the galaxies with high S_N are all fairly round ($\epsilon < 0.15$), independently of whether they are fast or slow rotators. Moreover, the galaxies with higher values of λ_R tend to have lower specific frequencies. To highlight this latter point, the bottom panel of Figure 13 plots S_N as function of λ_R . The apparent anticorrelation between these quantities is significant at the 94% confidence level; if galaxy #156 (the biggest outlier in Figure 11) were excluded, the significance would increase to 97%, although there is no *a priori* reason to exclude this galaxy. Such an anticorrelation between S_N and λ_R could occur if galaxies with low angular momentum experienced a larger number of dissipative mergers earlier in their history and formed greater numbers of GCs in the process, or it could indicate a lower M_*/M_h ratio in slow rotators, if N_{GC} scales reliably with halo mass.

4.4. Comparison of centroids of galaxy and GC system

Numerical simulations show that when galaxies interact, their dark matter halos are more affected than the stars (Mistani et al. 2016), which are much more centrally concentrated. However, because the GC system is spatially more extended than the field stars, the GCs are among the first stars to “notice” the interaction and undergo stripping if enough of the dark matter halo has been disrupted (Smith et al. 2013). This could be reflected as an asymmetrical shape and/or offset in the centroid of the GCs system with respect to the starlight. Such a displacement of the GC system has been found for a high-velocity early-type dwarf in the dense core of the Coma cluster (Cho et al. 2016), as well as for the cD NGC 4874 itself.

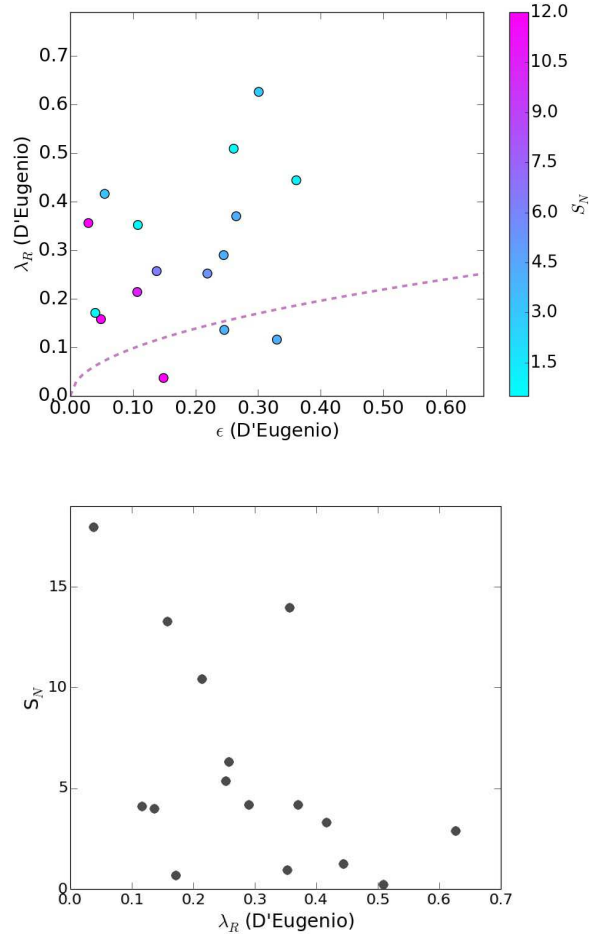


Figure 13. Top: projected specific angular momentum λ_R within R_e as function of galaxy ellipticity ϵ at R_e (data from D’Eugenio et al. 2013); the color code of the points indicate our measured S_N values. The highest S_N galaxies are preferentially round. Bottom: S_N plotted versus λ_R , suggesting a possible decreasing trend; the galaxy with $S_N = 14$ and $\lambda_R \approx 0.35$ is again #156.

To investigate whether the galaxies in A1689 show any evidence for offsets between the GCs and starlight, we calculate the clustercentric radial position of each galaxy (r_{Gal}) and its associated GC system (r_{GC}), based on the centroids given by the best-fit Sérsic models for each. We define $r = 0$ at the luminosity center of the cD galaxy, which coincides well with the geometrical center of the X-ray emission. We expect $r_{Gal} = r_{GC}$ for undisturbed galaxies. However, if the high- S_N central GC system is augmented by stripping GCs from cluster galaxies as they pass through the cluster core, we might expect $r_{Gal} > r_{GC}$ or $r_{Gal} < r_{GC}$, depending on the point in the orbit at which the galaxy is observed. Of course, local interactions with neighboring galaxies might also disrupt the extended GC distributions.

Figure 14 shows the histogram of offsets, where $r_{Gal} - r_{GC} > 0$ for galaxies with the fitted GC centroid closer to

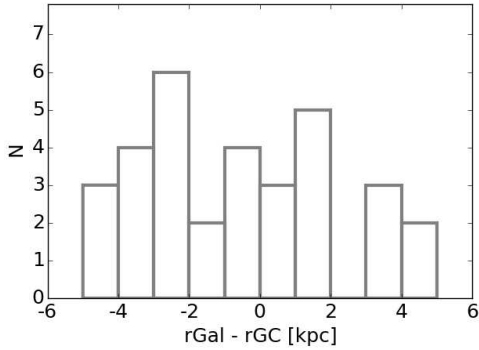


Figure 14. Top: Histogram of differences between galaxy and GC system central coordinates. Objects with $r_{\text{Gal}} - r_{\text{GC}} > 0$ have GC centroids displaced in the direction of the cluster center; those with and $r_{\text{Gal}} - r_{\text{GC}} < 0$ have GC centroids displaced away from the cluster center. The distribution appears fairly uniform; see text.

the cluster center and $r_{\text{Gal}} - r_{\text{GC}} < 0$ for galaxies with the GC system offset in the direction away from cluster center. While there are more galaxies with GC systems offset away from the cluster center, the difference is not significant. The distribution is quite uniform, without a strong peak at zero, likely indicating the limitations of our GC system centroiding as a consequence of the smoothing. However, we believe this is an interesting area for future studies with large samples of GC systems in rich nearby clusters such as Coma, where it is possible to reach farther along the GCLF, and the centroiding it not as limited by the resolution.

4.5. Comparison to A2744 Frontier Field

In AM13, we found that A1689 harbored $162,850^{+75,450}_{-51,300}$ GCs, integrated over the GCLF, within a projected radius of 400 kpc of the cluster center. As shown in Fig. 3 of AM13, the ACS/WFC areal coverage is incomplete to 400 kpc; the GCLF-integrated number within the ACS FOV is $153,600^{+71,200}_{-48,400}$. By analogy with other clusters, AM13 speculated that the total GC number within the virial radius of 3 Mpc may be several times larger, or $\sim 5 \times 10^5$. Based on these results, the A1689 GC population was the largest and most distant that had ever been studied. The error bars on the above values are dominated by the uncertainty on the GCLF extrapolation, which was based on M87 (Peng et al. 2009) translated to do the distances of A1689, with K corrections and 2.25 Gyr of passive evolution, and a GCLF width $\sigma = 1.4 \pm 0.1$ mag. Harris et al. (2017) advocated using $\sigma = 1.3 \pm 0.1$ mag for A1689 and similar cluster fields with a mix of early-type galaxies; adopting this value increases the extrapolated numbers by 29% to $198,000^{+91,800}_{-62,400}$ GCs within the ACS FOV.

The cluster A2744 which has a total mass of $\sim 2 \times 10^{15} M_{\odot}$ (Boschin et al. 2006) and $z = 0.308$, is the nearest of the Hubble Frontier Fields (Lotz et al. 2017), and the brightest members of its GC system are clearly visible (Blakeslee et al. 2015). Lee & Jang (2016; hereafter LJ16) reported

an extrapolated total of 385,000 GCs, with a quoted error of only 6%. These authors assumed the Milky Way GCLF with $\sigma = 1.2$ mag and that the observed F814W bandpass matched identically the rest-frame r -band. They did not report the actual number of detected GC candidates, but Harris et al. (2017), referencing a private communication, states that 664 GC candidates were detected (after completeness and contamination corrections) to $I_{814} = 29.0$ mag; this is on the Vega system and corresponds to $I_{814} = 29.4$ AB mag, or 4 mag brighter than the GCLF turnover adopted by LJ16. The extrapolated total based on these numbers exceeds 10^6 GCs, in contrast to what was reported by LJ16. Recognizing this, Harris et al. used a slightly revised set of GCLF parameters for A2744 with $\sigma = 1.3$ mag and derived a total of $3.9^{+7.2}_{-2.1} \times 10^5$ GCs, where the error bars now include realistic uncertainties on the GCLF and were calculated following the same prescription as in AM13. However, the assumed GCLF turnover magnitude was still not fully consistent with the value adopted for the A1689 extrapolation; using the same approach as in AM13, we estimate that the turnover should occur at an observed AB magnitude $I_{814} = 32.9 \pm 0.2$ mag. For $\sigma = 1.3 \pm 0.1$ mag, the extrapolation now gives $1.9^{+2.1}_{-0.9} \times 10^5$ GCs. With the brighter assumed turnover, the detections go 0.4σ farther along the GCLF, lessening the extrapolation; likewise, the error bars are smaller, in a fractional sense, than those reported by Harris et al. (2017).

Given the above estimates, one can only conclude that the number of GCs in A2744 appears similar to that found in A1689, but the value is much more poorly constrained for A2744, with an uncertainty range at least a factor of two larger. The fundamental reason is that AM13 detected more than ten times as many GC candidates in A1689, and the required extrapolation was a factor < 20 , rather than > 200 as in A2744. However, there are additional reasons for caution in interpreting the result for A2744. In the case of A1689, the AM13 analysis accounted for the effects of Eddington bias (which causes an overestimate of the true population), gravitational magnification of the background counts, and passive luminosity evolution; numbers were stated explicitly for the sizes of all these corrections. None of these issues were even mentioned by LJ16. Despite their quoted 6% uncertainty, LJ16 stated that their result was “a rough estimate of the total number of GCs in the Abell 2744 field.” We concur on this point, and conclude that the population of GCs in A1689 remains the largest that has been reliably measured to date. Future observations with the *James Webb Space Telescope* (JWST) should reveal even larger GC systems in other high density regions.

4.6. Core size and supermassive black hole mass

The favored explanation for the depletion of the light in the centers of massive “core” galaxies is the coalescence of binary supermassive black holes (SMBHs) in the final stages of galaxy merging, and the resultant “scouring” of stars on orbits that pass near the galaxy center. As the binary SMBHs orbit their common center of mass, stars interact and are

ejected from the system, removing angular momentum and causing the binary orbit to shrink (Begelman et al. 1980; Merritt & Milosavljević 2005). Numerical simulations of binary SMBHs predict that the amount of depleted mass correlates with the number of mergers and the total SMBH mass M_{BH} (Ebisuzaki et al. 1991; Merritt 2006).

There is an extensive body of work on empirical relations between M_{BH} and properties of the host galaxy (or its spheroidal component), such as luminosity, velocity dispersion (σ_v), Sérsic index, and N_{GC} (for reviews, see Ferrarese & Ford 2005; McConnell & Ma 2013; Kormendy & Ho 2013). Some simulations predict that the $M_{\text{BH}}-\sigma_v$ relation gets steeper at high masses (Boylan-Kolchin et al. 2006), and this was found observationally by McConnell et al. (2011), who reported the discovery of two SMBHs that were significantly more massive than predicted by the $M_{\text{BH}}-\sigma_v$ relation, suggesting a possibly different growth process at these high masses. Rusli et al. (2013) explored the relations between depleted stellar mass, core size, total luminosity, σ_v , and M_{BH} . They found that the strongest correlation for core galaxies was between R_b (as determined from core-Sérsic fitting) and M_{BH} , having the form:

$$\log\left(\frac{M_{\text{BH}}}{3 \times 10^9 M_{\odot}}\right) = (0.59 \pm 0.16) + (0.92 \pm 0.20) \log\left(\frac{R_b}{\text{kpc}}\right), \quad (5)$$

with a quoted intrinsic scatter of 0.28 dex in mass. From our best core-Sérsic fit, we obtain a core radius $R_b = 3.8 \pm 0.2$ kpc for the A1689 cD, which would imply an extraordinary SMBH mass $M_{\text{BH}} \approx (4 \pm 2) \times 10^{10} M_{\odot}$. However, the above empirical scaling is not constrained for $R_b > 1$ kpc or $M_{\text{BH}} > 2 \times 10^{10} M_{\odot}$. In fact, applying the somewhat steeper R_b - M_{BH} relation from Thomas et al. (2016) would imply an even more enormous M_{BH} , greater by a factor of two, even though the relations were fitted to essentially the same data and agree closely at $R_b < 1$ kpc. Thus, the safest conclusion is simply that M_{BH} likely exceeds $2 \times 10^{10} M_{\odot}$ in the A1689 BCG if its core has become depleted by the same physical process as in more nearby core galaxies for which M_{BH} has been measured.

Postman et al. (2012) used *HST* imaging to study the very large depleted core in the A2261 BCG, which they described as the largest known in any galaxy. Bonfini & Graham (2016) fitted the same data with a core-Sérsic model and determined $R_b = 3.6$ kpc, which they likewise characterized as the largest known. The latter authors suggested that depleted cores of such large sizes are formed by mechanisms other than scouring by binary black holes, including scouring by a gravitationally bound group of three or more SMBHs (Kulkarni & Loeb 2012), a scenario that might reasonably occur in a region as dense as the center of A1689. In the case of the A2261 BCG, there are multiple galactic nuclei visible within the break radius, and Bonfini & Graham suggest that the very large core more likely results from the dynamical effects of these massive luminous perturbers. We note that McNamara et al. (2009) reported a core radius of 3.8 kpc in the BCG of MS0735.6+7421, although this galaxy has significant dust in

its center, and Postman et al. (2009) claimed the value was overestimated by a factor of several. For A1689, there are no other luminous nuclei or obvious dust features within the cD's large break radius.

Another M_{BH} correlation that has been studied in the literature is with the total number of GCs in the host galaxy (Burkert & Tremaine 2010; Rhode et al. 2012; Harris et al. 2014). The most recent version has the form:

$$\log\left(\frac{M_{\text{BH}}}{M_{\odot}}\right) = (8.27 \pm 0.06) + (0.98 \pm 0.09) \log\left(\frac{N_{\text{GC}}}{500}\right) \quad (6)$$

with an intrinsic scatter of 0.30 dex in mass, after excluding galaxies classified as S0. For comparison, we calculate the M_{BH} predicted by the above relation using the GC population of the central galaxy obtained from our preferred two-component fit ($N_{\text{GC}} \approx 39,600$, see Figure 9), obtaining $M_{\text{BH}} \approx 1.4_{-0.7}^{+1.4} \times 10^{10} M_{\odot}$. However, if we consider the combined number of GCs from the BCG and intracluster components ($N_{\text{GC}} \approx 99,300$), the result is $M_{\text{BH}} \approx 3.3_{-1.7}^{+3.3} \times 10^{10} M_{\odot}$. Interestingly, the latter value agrees better with the estimate from R_b , but as in that case, we are again exploring an unprecedented regime requiring a large extrapolation. It would be extremely interesting to probe the limits of these empirical M_{BH} correlations by obtaining a dynamical mass for the SMBH in A1689. However, given the large distance and low central surface brightness, this is unlikely to be possible in the near future, even with the upcoming launch of *JWST*.

5. SUMMARY

We have modeled the light profiles of 180 galaxies near the center of A1689 using deep *HST*/ACS imaging, covering a physical area of approximately 600×600 kpc at $z = 0.183$. We fitted the galaxies using both single and double Sérsic models. Not surprisingly, the double Sérsic fits resulted in better residuals, and we adopted these for our final luminosity model. The photometric parameters from these fits are tabulated in an appendix. In order to model the luminosity profile of the central component, including both the BCG and ICL, we first subtracted the models for the 179 other galaxies, masked all other sources, and then fitted elliptical isophotes to the remaining light. We modeled the radial profile of the isophotes using a combination of a core-Sérsic model for the BCG and a more extended standard Sérsic for the ICL. Our preferred model used $n = 7$ for the Sérsic index of the BCG and gave a break radius $R_b = 3.8 \pm 0.2$ kpc, at the extreme high end found for break radii in core galaxies. The fitted Sérsic index for the ICL in this model was $n = 1.6$. We tried a range of fits, and concluded that the ICL represented $\sim 60\%$ of the light of the combined profile, although in the extreme cases, it could be as little as 23% or as much as 82%. This means that the ICL amounts to $11_{-7}^{+4}\%$ of the total A1689 stellar light within the FOV.

We followed a similar approach in modeling the GC systems of the galaxies, but it proved much more challenging because GCs represent less than 1% of the stellar light. As

a result, we were only able to obtain fits to the GC systems of 66 galaxies, and $\sim 25\%$ of these were rejected as unreliable; we included these “unreliable” fits in our complete model for the GC density map, but did not use them for estimating S_N values for the galaxies in question. We omitted another $\sim 25\%$ of the galaxies from the S_N analysis because they were uncertain cluster members or had poor luminosity fits, leaving a sample of 33 galaxies for which we have tabulated N_{GC} and S_N measurements. Only the nearby Virgo (Peng et al. 2008) and Fornax (Y. Liu, in preparation) clusters have had S_N measured for more individual galaxies. These A1689 galaxies are consistent with the trend of decreasing S_N with increasing luminosity found among giant ellipticals in Virgo and other nearby bright galaxy samples. However, a few galaxies at intermediate luminosities scatter to $S_N > 10$, and we are not able to reach lower luminosities where the S_N trend reverses.

The ICGCs in A1689 are difficult to disentangle from the GCs associated with the BCG. But, again following an analogous approach as used for the galaxy light, we find the ICGCs comprise $\sim 58\%$ of the combined population, or about 35% of the GCs over the whole field. This yields $S_N \approx 18$ for both the BCG and ICL. In this decomposition, 26% of the GCs are associated with the BCG, and the remaining 39% belong to non-central cluster galaxies in the FOV. We note that we have adopted the same GCLF as in AM13, and there is an additional uncertainty of about $\pm 35\%$ from the GCLF not included in the tabulated S_N measurement errors. In particular, adopting $\sigma = 1.3$ mag as advocated by Harris et al. (2017) increases our N_{GC} and S_N numbers by 29%.

Combining our results with kinematic measurements from D’Eugenio et al. (2013), we find that not all “slow rotators” have high S_N . Among the four galaxies with $S_N > 10$, only the BCG/cD is a clear slow rotator. However, all four of these galaxies are quite round, with ellipticities $\epsilon \lesssim 0.15$. In addition, there appears to be a trend, significant at the 94% level, of decreasing mean S_N with increasing specific angular momentum λ_R . These results are consistent with the observed trend of lower S_N in S0 galaxies as compared to giant ellipticals. An anticorrelation between S_N and λ_R might result

if galaxies with lower angular momenta experienced many dissipative mergers during their formation and consequently formed GCs with greater efficiency; alternatively, it could indicate a lower field star formation efficiency in slow rotators, if N_{GC} is a reliable tracer of halo mass.

We also reevaluated the GC population in A2744, the nearest of the Hubble Frontier Fields at $z \approx 0.31$. LJ16 claimed that it had the largest known population of GCs with a quoted uncertainty of only 6%. However, because of its larger distance, fewer than one-tenth as many GCs have been detected in A2744 as compared to A1689. Using a consistent set of assumptions for the GCLFs in these two clusters, we find similar extrapolated total GC numbers, but the uncertainty on the extrapolation is much greater for A2744. We conclude the GC population in A1689 remains the largest that has been reliably measured. This will be an interesting area to revisit with *JWST*.

The unusually large core in the A1689 BCG may hint at a central SMBH more massive than any yet detected by dynamical techniques in nearby galaxies. Published M_{BH} - R_b scaling relations are not empirically constrained at $R_b \gtrsim 1$ kpc, but a naive extrapolation to $R_b = 3.8$ kpc would imply $M_{BH} \sim 4 \times 10^{10} M_\odot$. We also calculated the SMBH mass implied by an extrapolation of the published scaling relation between M_{BH} and N_{GC} , although in this case there can be no causal connection. Because sizable extrapolations of the scaling relations are required in both cases, we simply conclude that $M_{BH} > 2 \times 10^{10} M_\odot$, if the core in this galaxy grew through the same processes that depleted the cores in nearby galaxies with measured SMBH masses. This is a question that likely must await high-resolution dynamical studies with the coming generation of extremely large telescopes.

K.A.M. acknowledges support from FONDECYT Postdoctoral Fellowship Project No. 3150599. We thank Bill Harris, Eric Peng, Thomas Puzia, Patrick Côté, and Laura Ferrarese for helpful discussions.

Facilities: HST (ACS/WFC)

APPENDIX

A. TABLES OF PHOTOMETRIC PARAMETERS AND SPECIFIC FREQUENCIES

Table 1 tabulates the Sérsic parameters for the 180 galaxies that we modeled in A1689. As discussed in Sec. 3.1, we estimate the error in total magnitude of each galaxy to be about 0.15 mag. Table 2 lists the total number of globular cluster N_{GC} , fitted Sérsic parameters, and specific frequency for each GC system in A1689 that we analyzed; the ID numbers can be used to match these GC system measurements with the photometric parameters for corresponding galaxies in Table 1.

Table 1. Galaxy Sérsic parameters

ID	RA	DEC	m_{F814}	m^{c1}	R_e^{c1}	n^{c1}	ϵ^{c1}	m^{c2}	R_e^{c2}	n^{c2}	ϵ^{c2}	cluster	flag
					[kpc]				[kpc]				
1	197.86360	-1.33608	17.4	17.6	5.6	0.7	0.06	19.7	1.1	1.2	0.02	n	1
4	197.85226	-1.34072	20.6	20.9	4.5	0.7	0.29	22.2	1.5	1.0	0.34	u	1
5	197.88098	-1.32576	16.8	16.9	5.1	1.4	0.21	19.4	1.0	0.7	0.14	y	1
6	197.85576	-1.34360	17.0	17.0	9.7	2.5	0.46	20.6	0.8	1.7	0.38	y	3
8	197.86307	-1.34953	18.9	19.4	4.4	0.5	0.49	19.9	1.8	0.7	0.60	y	2
9	197.88348	-1.34679	20.9	20.9	3.2	1.1	0.68	24.0	1.4	1.8	0.70	u	1
10	197.89201	-1.35052	17.9	18.1	4.3	1.9	0.60	19.6	4.0	4.0	0.60	y	3
12	197.89438	-1.36456	18.3	18.4	5.0	1.3	0.14	20.9	0.3	1.4	0.26	u	1
13	197.85151	-1.31046	19.3	20.2	4.0	0.5	0.60	19.9	2.6	4.0	0.58	y	1
15	197.87502	-1.34447	18.1	18.3	4.5	0.6	0.36	19.8	0.5	1.5	0.05	y	2
17	197.90275	-1.32853	19.1	19.9	2.4	5.6	0.40	19.8	3.1	0.8	0.20	y	2
18	197.86689	-1.34326	20.8	21.1	3.6	0.7	0.60	22.4	1.2	1.2	0.60	u	1
19	197.89844	-1.33672	18.4	18.5	4.3	0.7	0.19	20.7	0.1	4.0	0.30	y	3
20	197.86696	-1.32451	19.3	19.4	4.0	1.8	0.55	21.8	3.3	4.0	0.58	u	2
22	197.89740	-1.35921	17.7	18.0	5.6	1.2	0.60	19.2	0.8	1.7	0.30	y	2
23	197.86690	-1.31216	18.7	19.4	5.0	0.6	0.69	19.5	1.4	2.9	0.37	y	2
24	197.86216	-1.32797	19.5	20.9	5.6	0.5	0.00	19.9	3.4	2.1	0.68	u	2
25	197.86820	-1.31244	18.7	19.1	4.3	0.6	0.60	20.0	0.6	2.7	0.39	y	2
27	197.85645	-1.33895	21.0	22.3	2.0	1.6	0.35	21.4	2.2	0.7	0.15	u	1
28	197.87990	-1.31331	21.1	22.4	1.0	1.0	0.33	21.5	1.8	1.1	0.11	u	1
29	197.88623	-1.33292	16.3	16.8	10.0	1.5	0.39	17.6	1.6	2.4	0.21	y	1
30	197.88147	-1.32351	19.0	19.4	3.8	0.8	0.57	20.2	0.6	4.0	0.09	y	2
32	197.85839	-1.32649	19.6	21.5	2.5	0.5	0.21	19.8	2.7	2.9	0.07	y	1
33	197.88642	-1.32545	16.3	16.5	15.2	4.5	0.42	18.3	2.0	3.7	0.18	y	1
35	197.88095	-1.35931	20.1	20.7	7.2	3.2	0.60	21.1	1.9	0.5	0.54	u	1
36	197.87263	-1.34536	19.5	19.9	2.5	0.5	0.36	20.7	0.3	2.1	0.14	u	3
38	197.87536	-1.34522	16.4	16.5	12.9	6.0	0.16	19.4	5.1	0.5	0.10	y	2
39	197.86988	-1.31737	19.1	19.8	4.1	0.7	0.39	19.9	1.3	4.0	0.46	y	1
40	197.88324	-1.34428	19.8	20.1	4.6	0.8	0.44	21.3	0.7	2.0	0.26	u	1
41	197.87525	-1.34123	17.3	17.8	7.3	0.8	0.20	18.3	1.5	1.4	0.22	y	2
42	197.86826	-1.33290	18.0	18.3	2.9	4.3	0.44	19.5	5.1	0.7	0.58	y	2
43	197.87130	-1.36038	18.6	18.9	3.7	0.9	0.60	20.1	0.5	1.4	0.30	y	3
44	197.88038	-1.33774	19.7	19.8	3.6	3.5	0.60	23.2	0.6	1.1	0.60	u	2

Table 1 continued

Table 1 (continued)

ID	RA	DEC	m_{F814}	m^{c1}	R_e^{c1}	n^{c1}	ϵ^{c1}	m^{c2}	R_e^{c2}	n^{c2}	ϵ^{c2}	cluster	flag
					[kpc]				[kpc]			member	
45	197.87314	-1.35459	20.7	21.6	4.0	0.7	0.23	21.2	1.3	1.5	0.13	u	1
46	197.86932	-1.34069	18.4	18.5	6.1	3.2	0.48	21.8	0.3	1.7	0.18	y	2
47	197.87417	-1.33881	20.0	21.4	1.8	0.6	0.27	20.4	5.1	4.0	0.48	u	1
48	197.88292	-1.31491	18.9	19.2	2.6	4.8	0.09	20.7	3.8	0.6	0.13	y	1
49	197.84620	-1.35477	18.5	18.8	4.1	1.3	0.60	19.9	0.4	2.9	0.23	y	3
50	197.87263	-1.31180	20.1	21.8	1.3	0.8	0.39	20.4	5.1	1.3	0.60	u	3
51	197.86033	-1.32997	19.6	20.0	3.0	0.9	0.36	20.7	0.8	2.9	0.37	y	1
52	197.90840	-1.32801	19.4	19.7	3.4	3.7	0.59	21.0	2.8	1.5	0.60	u	1
53	197.87004	-1.35046	20.1	20.7	2.3	1.2	0.60	21.1	2.7	4.0	0.46	u	3
54	197.87458	-1.33752	19.0	20.6	3.8	0.5	0.58	19.2	2.5	4.0	0.30	y	2
55	197.86794	-1.33212	21.0	21.5	1.0	1.5	0.14	22.0	3.9	0.5	0.60	u	3
56	197.87754	-1.34546	17.8	18.1	2.1	3.1	0.07	19.2	5.1	0.7	0.30	y	2
57	197.87279	-1.32510	19.7	20.9	2.0	0.5	0.41	20.2	2.5	4.0	0.47	u	1
58	197.87144	-1.36533	18.1	18.6	2.4	3.7	0.38	19.3	5.1	1.6	0.15	y	1
59	197.87688	-1.31791	20.5	21.9	1.9	0.8	0.60	20.8	3.3	1.7	0.19	u	3
60	197.86766	-1.34539	17.6	17.7	7.2	2.3	0.17	19.7	0.6	2.0	0.22	y	2
61	197.86944	-1.35081	20.2	20.9	5.1	0.5	0.38	21.1	1.6	1.4	0.46	u	1
62	197.87163	-1.35573	20.8	22.0	0.7	2.2	0.06	21.3	2.3	0.6	0.11	u	1
63	197.87098	-1.35464	17.6	17.9	6.4	2.3	0.03	19.4	0.9	2.1	0.33	y	1
64	197.85024	-1.31872	18.7	19.0	5.4	6.0	0.42	20.1	5.1	2.0	0.59	y	1
65	197.87606	-1.34771	18.0	18.2	2.9	1.2	0.18	19.5	0.4	1.2	0.06	y	1
66	197.87121	-1.34472	20.5	21.7	1.0	2.0	0.22	20.9	2.3	1.2	0.12	u	1
67	197.87983	-1.35697	17.4	17.5	8.4	4.0	0.11	20.1	0.6	4.0	0.21	y	2
68	197.88386	-1.36057	17.9	19.6	11.6	0.8	0.60	18.1	2.8	4.0	0.25	y	2
69	197.85814	-1.33107	18.2	18.3	2.3	3.5	0.23	20.9	5.1	4.0	0.60	y	2
70	197.86637	-1.36018	18.7	18.9	3.0	1.1	0.60	20.4	0.3	1.5	0.17	y	3
71	197.87630	-1.34143	17.0	17.6	5.6	0.7	0.06	18.1	1.1	2.1	0.05	y	2
72	197.90779	-1.32237	17.1	17.3	4.5	5.1	0.05	18.9	3.4	4.0	0.27	y	2
73	197.89215	-1.35517	18.9	19.3	3.2	1.3	0.60	20.1	0.7	2.6	0.22	y	3
74	197.86295	-1.31333	19.9	21.9	3.2	0.5	0.40	20.1	2.6	3.3	0.28	y	1
75	197.86387	-1.31076	20.3	21.3	3.3	0.5	0.41	20.8	1.2	1.7	0.49	u	2
76	197.88723	-1.36132	19.6	19.7	2.5	2.9	0.43	24.4	1.7	0.5	0.60	u	1
77	197.86614	-1.35358	18.9	19.5	3.2	1.1	0.26	19.8	0.6	3.4	0.16	y	2
78	197.87653	-1.35320	20.3	21.3	1.1	1.8	0.27	20.9	2.2	0.8	0.30	u	2

Table 1 continued

Table 1 (continued)

ID	RA	DEC	m_{F814}	m^{c1}	R_e^{c1}	n^{c1}	ϵ^{c1}	m^{c2}	R_e^{c2}	n^{c2}	ϵ^{c2}	cluster	flag
					[kpc]				[kpc]			member	
79	197.86341	-1.34264	20.1	21.6	1.9	0.8	0.53	20.4	3.1	4.0	0.37	u	1
81	197.87489	-1.33220	18.5	18.6	2.0	2.0	0.06	20.9	0.4	1.9	0.06	y	1
82	197.84903	-1.34259	20.6	21.1	2.3	3.0	0.60	21.7	2.0	0.6	0.60	u	2
83	197.88260	-1.34962	18.5	18.7	4.1	6.0	0.15	20.7	5.0	1.0	0.42	y	1
84	197.85195	-1.35305	18.0	19.6	6.2	6.0	0.35	18.2	2.9	4.0	0.60	y	2
85	197.88627	-1.34956	19.8	20.4	3.1	1.4	0.37	20.7	1.0	3.5	0.47	u	1
86	197.89496	-1.34977	18.2	18.8	4.0	1.5	0.43	19.3	0.8	1.9	0.19	y	2
87	197.87208	-1.33173	19.9	20.2	3.8	2.2	0.51	21.6	0.7	2.1	0.37	u	1
88	197.88258	-1.32079	19.9	20.3	1.3	2.1	0.45	21.1	3.5	0.6	0.33	u	1
89	197.87876	-1.34360	21.0	22.5	1.0	3.3	0.47	21.3	1.3	0.7	0.16	u	2
90	197.87889	-1.34106	19.8	19.9	2.2	1.2	0.60	21.9	0.5	1.7	0.47	u	2
91	197.86058	-1.31772	19.4	19.8	2.1	5.5	0.34	20.7	2.3	0.7	0.52	y	2
92	197.88435	-1.33586	21.0	21.3	1.7	1.3	0.24	22.6	1.3	1.2	0.60	u	1
93	197.84260	-1.35661	19.0	19.5	1.0	6.0	0.40	20.0	2.2	0.5	0.31	u	2
94	197.89081	-1.32523	21.1	21.7	1.9	1.8	0.66	21.9	1.7	1.7	0.64	u	1
95	197.88344	-1.32341	18.1	20.5	1.0	6.0	0.26	18.2	2.7	3.6	0.23	y	1
96	197.89665	-1.35353	19.1	19.4	2.6	1.8	0.29	20.8	0.5	1.4	0.13	y	1
97	197.89070	-1.31860	21.1	21.5	2.9	1.6	0.58	22.3	1.0	1.4	0.60	u	1
98	197.86606	-1.33547	17.5	17.9	4.2	1.4	0.06	18.8	0.5	1.6	0.02	y	1
99	197.87315	-1.33999	21.1	21.1	1.5	1.8	0.14	-	-	-	-	u	1
100	197.89361	-1.37080	19.1	19.6	12.9	3.4	0.06	20.2	1.2	2.3	0.02	u	1
101	197.85506	-1.32141	20.6	21.2	1.3	1.3	0.01	21.4	2.7	4.0	0.06	u	1
102	197.87199	-1.36153	21.2	23.4	4.5	0.5	0.46	21.3	1.4	1.1	0.28	u	3
103	197.88728	-1.34736	20.5	20.8	1.7	1.9	0.37	22.0	3.3	4.0	0.28	u	1
104	197.88429	-1.36964	17.4	17.5	15.2	5.9	0.28	19.4	1.0	3.2	0.23	y	2
105	197.89068	-1.32743	20.0	20.7	3.9	6.0	0.60	20.7	1.6	1.0	0.60	n	2
106	197.88396	-1.32965	17.5	18.4	5.8	0.5	0.11	18.2	1.1	2.7	0.07	y	2
107	197.85240	-1.34852	20.0	20.2	2.0	2.5	0.18	21.9	0.9	2.1	0.29	u	1
108	197.86452	-1.32156	20.7	22.3	1.7	0.5	0.14	20.9	1.4	2.6	0.31	u	1
109	197.84447	-1.36221	20.9	21.0	1.4	1.8	0.44	22.9	2.8	0.5	0.21	u	1
110	197.87510	-1.36870	17.9	18.5	9.6	1.1	0.49	18.9	1.0	2.6	0.29	y	1
111	197.86220	-1.32689	17.8	18.5	14.8	0.5	0.54	18.6	1.7	4.0	0.21	y	2
112	197.90224	-1.32363	20.4	20.8	4.3	1.8	0.47	21.7	0.7	2.2	0.47	n	1
113	197.85781	-1.30941	19.8	20.6	2.4	1.1	0.04	20.5	0.7	3.4	0.00	u	1

Table 1 continued

Table 1 (continued)

ID	RA	DEC	m_{F814}	m^{c1}	R_e^{c1}	n^{c1}	ϵ^{c1}	m^{c2}	R_e^{c2}	n^{c2}	ϵ^{c2}	cluster	flag
					[kpc]				[kpc]			member	
114	197.86104	-1.33803	20.8	20.9	1.5	2.0	0.11	23.9	1.1	4.0	0.48	u	1
115	197.86573	-1.33767	20.3	20.9	1.9	0.6	0.26	21.1	0.6	2.3	0.37	u	1
116	197.88895	-1.32858	18.8	19.9	5.5	0.5	0.46	19.4	0.9	2.5	0.09	y	2
117	197.85933	-1.33234	18.1	18.3	1.6	2.9	0.41	19.9	5.1	2.0	0.15	y	1
118	197.88466	-1.31970	20.7	20.8	1.8	1.4	0.60	24.7	0.1	0.5	0.38	u	2
119	197.90482	-1.32604	20.9	21.1	1.8	1.9	0.23	22.7	0.9	0.5	0.29	u	1
120	197.87926	-1.35771	19.0	19.4	1.3	3.0	0.27	20.5	4.0	0.5	0.50	y	2
121	197.89499	-1.32348	18.6	18.8	1.7	4.4	0.12	20.6	5.1	0.5	0.28	y	2
122	197.86949	-1.34689	21.3	22.5	2.1	0.5	0.21	21.7	0.9	1.3	0.36	u	1
123	197.89743	-1.33805	20.9	21.5	2.1	3.0	0.60	21.9	1.5	1.7	0.59	u	1
124	197.87127	-1.35993	20.5	21.2	3.0	0.6	0.60	21.2	1.0	1.6	0.26	y	3
125	197.89716	-1.32137	21.2	22.1	1.0	1.8	0.43	21.9	2.5	1.6	0.60	u	1
127	197.89266	-1.32036	20.9	22.4	2.4	0.8	0.08	21.3	1.2	2.8	0.36	u	1
128	197.84925	-1.34023	19.8	19.8	2.2	4.9	0.03	24.5	0.5	0.5	0.49	u	1
129	197.89676	-1.35528	18.6	18.6	2.1	4.1	0.23	21.9	1.2	0.5	0.60	y	1
130	197.87844	-1.34186	18.0	18.2	7.3	6.0	0.15	19.8	1.3	3.1	0.50	y	2
131	197.86318	-1.31808	19.1	19.5	5.8	6.0	0.15	20.3	1.5	2.6	0.59	y	2
132	197.89754	-1.34519	18.3	18.7	3.5	3.1	0.09	19.6	0.6	4.0	0.04	y	1
133	197.85740	-1.34258	20.0	21.9	1.8	6.0	0.34	20.2	1.6	1.5	0.59	u	3
134	197.86424	-1.33401	18.1	18.9	6.0	1.2	0.05	18.9	1.0	4.0	0.24	y	1
135	197.87232	-1.31881	20.2	20.2	1.6	1.9	0.54	23.9	0.2	0.7	0.24	u	1
136	197.89539	-1.33456	19.1	19.9	3.4	0.6	0.38	19.8	0.5	3.0	0.29	y	1
137	197.87269	-1.33644	21.0	21.1	1.2	1.1	0.13	23.9	0.1	1.2	0.04	u	1
138	197.89822	-1.35255	19.0	20.0	4.2	0.5	0.13	19.6	0.8	2.8	0.26	y	2
139	197.87416	-1.31256	21.1	21.1	1.4	1.2	0.56	-	-	-	-	u	2
140	197.87964	-1.34792	18.5	18.9	2.2	1.0	0.08	19.7	0.3	1.6	0.03	y	1
142	197.86495	-1.34294	20.8	21.8	1.0	2.6	0.50	21.4	1.2	0.9	0.13	u	1
143	197.87410	-1.35017	18.9	19.2	1.0	3.8	0.13	20.6	3.9	0.5	0.24	y	1
144	197.87809	-1.36978	20.7	21.8	2.6	0.7	0.42	21.2	0.9	1.4	0.60	u	1
145	197.84153	-1.35485	21.2	21.4	1.0	1.7	0.33	22.9	2.2	0.5	0.16	u	1
146	197.86722	-1.32543	18.4	18.8	1.0	4.1	0.25	19.7	5.1	0.8	0.60	y	2
148	197.87969	-1.35771	18.1	18.2	1.6	3.3	0.24	21.1	4.6	0.5	0.60	y	2
149	197.86556	-1.35226	20.8	22.1	1.2	0.5	0.01	21.3	0.6	1.7	0.29	y	3
150	197.88038	-1.36321	21.0	21.1	1.4	1.7	0.48	24.8	0.3	3.6	0.60	u	1

Table 1 continued

Table 1 (*continued*)

ID	RA	DEC	m_{F814}	m^{c1}	R_e^{c1}	n^{c1}	ϵ^{c1}	m^{c2}	R_e^{c2}	n^{c2}	ϵ^{c2}	cluster	flag
					[kpc]				[kpc]			member	
151	197.89948	-1.33262	19.4	19.5	2.3	3.6	0.36	21.8	0.7	0.5	0.49	y	1
152	197.86628	-1.36595	19.6	19.7	1.6	1.7	0.60	21.9	0.3	1.9	0.60	u	1
153	197.84824	-1.35306	21.1	24.5	3.8	0.5	0.37	21.2	1.3	1.5	0.60	u	2
154	197.87287	-1.36927	21.3	21.4	1.0	1.5	0.43	23.8	2.2	0.5	0.27	u	2
155	197.85585	-1.33810	18.6	19.3	10.5	0.8	0.34	19.4	1.0	4.0	0.16	y	2
156	197.85475	-1.32528	18.6	18.8	5.3	3.5	0.09	20.2	0.4	4.0	0.41	y	1
157	197.88115	-1.35167	20.7	20.8	1.2	2.0	0.39	24.0	0.6	4.0	0.60	y	1
158	197.87148	-1.31401	20.5	20.9	5.7	6.0	0.23	22.0	1.3	2.6	0.30	u	1
159	197.87676	-1.34301	19.1	20.3	3.1	0.8	0.47	19.5	0.8	2.0	0.40	y	2
160	197.86885	-1.34174	20.4	21.3	1.0	2.1	0.42	21.1	2.6	2.8	0.60	u	2
161	197.87671	-1.34594	18.1	21.8	1.0	2.4	0.37	18.2	1.7	4.0	0.14	y	1
162	197.84011	-1.36156	19.6	20.4	2.3	1.3	0.13	20.3	0.5	4.0	0.13	y	1
163	197.87094	-1.34828	18.7	18.8	1.1	2.8	0.24	21.6	1.5	0.5	0.47	y	2
164	197.87850	-1.34863	20.5	20.8	1.3	2.1	0.31	22.0	1.1	0.7	0.60	y	2
165	197.86525	-1.36081	20.1	21.3	2.8	1.2	0.09	20.5	1.0	1.8	0.60	u	2
166	197.87250	-1.34941	20.6	21.9	1.2	0.8	0.37	21.1	0.9	2.1	0.33	u	2
167	197.87493	-1.31782	20.3	20.9	1.3	2.1	0.30	21.2	0.8	1.0	0.22	u	2
168	197.85088	-1.35207	18.8	19.5	2.8	1.0	0.12	19.5	0.4	2.9	0.14	y	2
169	197.89110	-1.33224	20.1	20.6	1.0	4.1	0.21	21.2	1.9	1.7	0.59	u	2
170	197.87456	-1.32530	20.9	22.0	1.8	1.1	0.07	21.4	0.8	1.9	0.56	u	1
171	197.87530	-1.36194	18.1	18.9	13.5	5.6	0.22	18.8	1.1	3.6	0.60	y	1
172	197.87222	-1.32127	18.5	20.9	7.9	0.5	0.60	18.6	1.3	3.0	0.60	y	3
173	197.87513	-1.34275	20.5	21.1	1.7	0.6	0.57	21.4	0.4	2.0	0.52	u	2
174	197.87526	-1.35504	19.0	20.1	1.0	6.0	0.22	19.5	1.1	1.7	0.37	y	2
175	197.87668	-1.35269	20.2	20.5	4.2	6.0	0.47	21.6	0.7	4.0	0.52	u	3
176	197.86865	-1.34030	18.1	18.2	3.7	6.0	0.08	20.6	0.5	0.8	0.17	y	2
177	197.87036	-1.33387	21.1	21.6	1.2	1.3	0.08	22.2	0.6	2.1	0.50	y	1
178	197.88933	-1.32345	20.3	21.2	1.5	0.8	0.17	21.0	0.3	4.0	0.16	u	2
179	197.87228	-1.35152	19.5	20.7	1.2	0.8	0.28	19.9	0.7	4.0	0.21	y	1
180	197.86765	-1.36779	20.9	21.2	1.0	1.4	0.27	22.7	0.5	1.2	0.60	y	1
181	197.87367	-1.36065	21.2	22.2	1.8	1.1	0.22	21.7	0.6	1.5	0.50	u	1
182	197.87992	-1.34560	19.4	20.5	2.4	0.7	0.07	19.8	0.4	2.0	0.10	y	2
183	197.87516	-1.33814	19.2	19.7	6.9	4.2	0.60	20.1	0.4	3.1	0.26	y	1
184	197.88871	-1.36590	20.8	21.1	1.2	4.9	0.07	22.4	0.5	1.3	0.10	u	1

Table 1 continued

Table 1 (*continued*)

ID	RA	DEC	m_{F814}	m^{c1}	R_e^{c1}	n^{c1}	ϵ^{c1}	m^{c2}	R_e^{c2}	n^{c2}	ϵ^{c2}	cluster	flag
					[kpc]				[kpc]				
185	197.89166	-1.37136	20.3	20.6	1.0	2.0	0.16	21.9	0.2	3.4	0.22	u	1
186	197.87828	-1.31459	20.1	20.9	1.3	1.6	0.33	20.9	0.4	3.4	0.60	y	1
187	197.87125	-1.32970	19.4	19.8	1.4	1.7	0.60	20.6	0.2	3.5	0.11	y	2
188	197.87534	-1.36657	20.5	20.8	1.1	6.0	0.05	22.3	0.5	1.1	0.51	u	2
189	197.87044	-1.33282	21.4	22.3	1.0	0.7	0.11	22.0	0.3	3.5	0.08	u	1
190	197.87226	-1.34055	20.2	21.4	1.0	6.0	0.50	20.6	0.6	1.2	0.14	u	2
191	197.88846	-1.32137	20.3	21.0	1.0	6.0	0.05	21.1	0.5	1.5	0.11	y	1
192	197.87580	-1.34155	20.1	20.7	3.5	0.6	0.60	20.9	0.4	2.4	0.07	y	2
193	197.88103	-1.31603	21.0	21.8	1.0	6.0	0.42	21.7	0.5	1.3	0.15	u	1
194	197.87643	-1.34060	20.8	21.4	1.1	6.0	0.54	21.6	0.3	2.0	0.24	y	1
cD	197.87297	-1.34110	15.7	15.7	8.3	7.0	-	-	-	-	-	y	1

NOTE—Best fit parameters for the 2-D double component Sérsic models for the first 179 galaxies. The R_e 's are major-axis values. For galaxies #99 and #139 the second component had null contribution. The cD parameters are the 1-D single core-Sérsic fit, with $R_b = 3.8$ kpc, $\gamma = 0.04$ and $\alpha=2.6$; R_e and R_b are circularized values. The cluster member column indicates if the galaxy is a confirmed member (y), known non-member (n), or unknown (u).

Flag 1 (good) and 2 (acceptable) are reliable fits, while 3 indicates the fit is unreliable.

Table 2. Globular cluster system Sérsic parameters

ID	N_{GC}	R_e^{GC} [kpc]	Sérsic index	S_N
5	4142 ± 284	19.0	4.0	5.4 ± 1.1
29	4858 ± 307	29.5	4.0	4.1 ± 0.8
33	4858 ± 307	33.1	4.0	4.0 ± 0.8
51	50 ± 31	8.8	4.0	0.8 ± 0.6
56	706 ± 117	3.4	1.6	2.2 ± 0.7
58	1337 ± 162	13.0	0.7	5.9 ± 1.5
60	1221 ± 154	8.6	4.0	3.2 ± 0.8
63	4858 ± 307	21.1	2.2	13.3 ± 2.7
65	2032 ± 199	9.1	1.5	7.7 ± 1.8
67	3408 ± 257	30.9	4.0	7.8 ± 1.7
68	1218 ± 155	18.5	4.0	4.2 ± 1.1
69	881 ± 132	10.3	4.0	4.2 ± 1.2

Table 2 continued

Table 2 (*continued*)

ID	N_{GC}	R_e^{GC} [kpc]	Sérsic index	S_N
72	415 ± 91	17.1	4.0	0.7 ± 0.3
86	600 ± 109	11.0	4.0	2.9 ± 0.9
96	405 ± 90	5.7	0.9	4.5 ± 1.6
98	2529 ± 221	12.4	4.0	6.3 ± 1.4
106	2086 ± 201	12.6	4.0	5.3 ± 1.3
111	1924 ± 194	33.6	2.3	6.3 ± 1.5
116	360 ± 84	8.6	4.0	3.0 ± 1.1
117	301 ± 78	1.1	0.5	1.3 ± 0.5
120	50 ± 31	8.0	4.0	0.5 ± 0.4
121	142 ± 55	8.8	4.0	0.9 ± 0.5
129	449 ± 95	8.2	4.0	3.0 ± 1.0
132	369 ± 87	10.5	1.5	1.9 ± 0.7
134	2362 ± 214	13.9	4.0	10.4 ± 2.4
140	538 ± 103	6.0	0.9	3.3 ± 1.1
148	50 ± 31	6.7	1.8	0.2 ± 0.2
151	171 ± 60	8.4	4.0	2.4 ± 1.2
155	150 ± 56	3.0	4.0	1.0 ± 0.5
156	2131 ± 204	16.6	3.4	14.0 ± 3.3
161	1461 ± 168	6.7	4.0	6.4 ± 1.6
171	1681 ± 181	28.6	1.3	7.4 ± 1.8
cD	39574 ± 11872	39.7	1.0	18.0 ± 9.0
ICL	53679 ± 16104	172.0	1.0	16.9 ± 6.0

NOTE—Best 2-D single Sérsic models for the confirmed A1689 members and classified as reliable fits. N_{GC} is the total number after correcting for incompleteness, background contamination, uncovered areas, and GCLF. The values for the cD and ICL are from 1-D core-Sérsic and Sérsic , respectively.

REFERENCES

- Abell, G. O. 1965, ARA&A, 3, 1
- Alamo-Martínez, K. A., Blakeslee, J. P., Jee, M. J., et al. 2013, ApJ, 775, 20 (AM13)
- Anderson, J., & Bedin, L. R. 2010, PASP, 122, 1035
- Baldry, I. K., Balogh, M. L., Bower, R. G., et al. 2006, MNRAS, 373, 469
- Balogh, M. L., McGee, S. L., Mok, A., et al. 2016, MNRAS, 456, 4364
- Beers, T. C., Flynn, K., & Gebhardt, K. 1990, AJ, 100, 32
- Begelman, M. C., Blandford, R. D., & Rees, M. J. 1980, Nature, 287, 307
- Bender, R. 1988, A&A, 193, L7
- Bender, R., Surma, P., Doebereiner, S., Moellenhoff, C., & Madejsky, R. 1989, A&A, 217, 35
- Bender, R., Kormendy, J., Cornell, M. E., & Fisher, D. B. 2015, ApJ, 807, 56
- Bertin, E., & Arnouts, S. 1996, A&AS, 117, 393
- Blakeslee, J. P. 1999, AJ, 118, 1506

- Blakeslee, J. P., Alamo-Martinez, K., Toloba, E., Barro, G., & Peng, E. W. 2015, American Astronomical Society Meeting Abstracts, 225, 252.09
- Blakeslee, J. P., Anderson, K. R., Meurer, G. R. et al. 2003, *Astronomical Data Analysis Software and Systems XII* (ASP Conf. Ser. 295), ed. H. E. Payne, R. I. Jedrzejewski, & R. N. Hook (San Francisco, CA: ASP), 257
- Blakeslee, J. P., Holden, B. P., Franx, M., et al. 2006, *ApJ*, 644, 30
- Blakeslee, J. P., Tonry, J. L., & Metzger, M. R. 1997, *AJ*, 114, 482
- Bluck, A. F. L., Mendel, J. T., Ellison, S. L., et al. 2016, *MNRAS*, 462, 2559
- Bonfini, P., & Graham, A. W. 2016, *ApJ*, 829, 81
- Boschin, W., Girardi, M., Spolaor, M., & Barrena, R. 2006, *A&A*, 449, 461
- Boylan-Kolchin, M., Ma, C.-P., & Quataert, E. 2006, *MNRAS*, 369, 1081
- Brodie, J. P., & Strader, J. 2006, *ARA&A*, 44, 193
- Burkert, A., & Tremaine, S. 2010, *ApJ*, 720, 516
- Cappellari, M., Emsellem, E., Krajnović, D., et al. 2011, *MNRAS*, 416, 1680
- Cho, H., Blakeslee, J. P., Chies-Santos, A. L., et al. 2016, *ApJ*, 822, 95
- Chung, A., van Gorkom, J. H., Kenney, J. D., Crawl, H., & Vollmer, B. 2009, *AJ*, 138, 1741
- Côté, P., Blakeslee, J. P., Ferrarese, L., et al. 2004, *ApJS*, 153, 223
- Contini, E., De Lucia, G., Villalobos, Á., & Borgani, S. 2014, *MNRAS*, 437, 3787
- Cooper, A. P., Gao, L., Guo, Q., et al. 2015, *MNRAS*, 451, 2703
- D'Eugenio, F., Houghton, R. C. W., Davies, R. L., & Dalla Bontà, E. 2013, *MNRAS*, 429, 1258
- Donzelli, C. J., Muriel, H., & Madrid, J. P. 2011, *ApJS*, 195, 15
- Dressler, A. 1980, *ApJ*, 236, 351
- Durrell, P. R., Côté, P., Peng, E. W., et al. 2014, *ApJ*, 794, 103
- Ebisuzaki, T., Makino, J., & Okumura, S. K. 1991, *Nature*, 354, 212
- Einasto, J., Saar, E., Kaasik, A., & Chernin, A. D. 1974, *Nature*, 252, 111
- Emsellem, E., Cappellari, M., Krajnović, D., et al. 2007, *MNRAS*, 379, 401
- Emsellem, E., Cappellari, M., Krajnović, D., et al. 2011, *MNRAS*, 414, 888
- Ferrarese, L., Côté, P., Jordán, A., et al. 2006, *ApJS*, 164, 334
- Ferrarese, L., & Ford, H. 2005, *SSRv*, 116, 523
- Fossati, M., Wilman, D. J., Mendel, J. T., et al. 2017, *ApJ*, 835, 153
- Gallagher, J. S., III, & Ostriker, J. P. 1972, *AJ*, 77, 288
- Georgiev, I. Y., Puzia, T. H., Goudfrooij, P., & Hilker, M. 2010, *MNRAS*, 406, 1967
- Gonzalez, A. H., Zabludoff, A. I., & Zaritsky, D. 2005, *ApJ*, 618, 195
- Graham, A. W., Erwin, P., Trujillo, I., & Asensio Ramos, A. 2003, *AJ*, 125, 2951
- Graham, A. W., & Driver, S. P. 2005, *PASA*, 22, 118
- Halkola, A., Seitz, S., & Pannella, M. 2006, *MNRAS*, 372, 1425 (H06)
- Harris, W. E. 1991, *ARA&A*, 29, 543
- Harris, W. E. 2001, in *Star Clusters*, Saas-Fee Advanced Courses, Vol. 28, ed. L. Labhardt & B. Binggeli (Berlin: Springer), 223
- Harris, W. E., Blakeslee, J. P., & Harris, G. L. H. 2017, *ApJ*, 836, 67
- Harris, G. L. H., Poole, G. B., & Harris, W. E. 2014, *MNRAS*, 438, 2117
- Harris, W. E., Harris, G. L. H., & Alessi, M. 2013, *ApJ*, 772, 82
- Harris, W. E., & van den Bergh, S. 1981, *AJ*, 86, 1627
- Hudson, M. J., Gillis, B. R., Coupon, J., et al. 2015, *MNRAS*, 447, 298
- Hudson, M. J., Harris, G. L., & Harris, W. E. 2014, *ApJL*, 787, L5
- Jaffé, Y. L., Verheijen, M. A. W., Haines, C. P., et al. 2016, *MNRAS*, 461, 1202
- Jordán, A., West, M. J., Côté, P., & Marzke, R. O. 2003, *AJ*, 125, 1642
- Kauffmann, G., White, S. D. M., Heckman, T. M., et al. 2004, *MNRAS*, 353, 713
- Knobel, C., Lilly, S. J., Woo, J., & Kovač, K. 2015, *ApJ*, 800, 24
- Ko, Y., Hwang, H. S., Lee, M. G., et al. 2017, *ApJ*, 835, 212
- Komatsu, E., Smith, K. M., Dunkley, J., et al. 2011, *ApJS*, 192, 18
- Kormendy, J., Fisher, D. B., Cornell, M. E., & Bender, R. 2009, *ApJS*, 182, 216
- Kormendy, J., & Ho, L. C. 2013, *ARA&A*, 51, 511
- Kravtsov, A. V., & Gnedin, O. Y. 2005, *ApJ*, 623, 650
- Kulkarni, G., & Loeb, A. 2012, *MNRAS*, 422, 1306
- Lagos, C. D. P., Lacey, C. G., Baugh, C. M., Bower, R. G., & Benson, A. J. 2011, *MNRAS*, 416, 1566
- Lee, M. G., & Jang, I. S. 2016, *ApJ*, 831, 108 (LJ16)
- Liu, Y., Peng, E. W., Blakeslee, J., et al. 2016, *ApJ*, 818, 179
- López-Cruz, O., Añorve, C., Birkinshaw, M., et al. 2014, *ApJL*, 795, L31
- Lotz, J. M., Koekemoer, A., Coe, D., et al. 2017, *ApJ*, 837, 97
- Mackey, A. D., Beasley, M. A., & Leaman, R. 2016, *MNRAS*, 460, L114
- Madrid, J. P., & Donzelli, C. J. 2016, *ApJ*, 819, 50
- Mandelbaum, R., Seljak, U., Kauffmann, G., Hirata, C. M., & Brinkmann, J. 2006, *MNRAS*, 368, 715
- Matthews, T. A., Morgan, W. W., & Schmidt, M. 1964, *ApJ*, 140, 35
- McConnell, N. J., & Ma, C.-P. 2013, *ApJ*, 764, 184
- McConnell, N. J., Ma, C.-P., Gebhardt, K., et al. 2011, *Nature*, 480, 215
- McNamara, B. R., Kazemzadeh, F., Rafferty, D. A., et al. 2009, *ApJ*, 698, 594

- Merritt, D., & Milosavljević, M. 2005, *Living Reviews in Relativity*, 8
- Merritt, D. 2006, *ApJ*, 648, 976
- Mihos, J. C., Harding, P., Feldmeier, J., & Morrison, H. 2005, *ApJL*, 631, L41
- Mihos, J. C., Harding, P., Feldmeier, J. J., et al. 2017, *ApJ*, 834, 16
- Mistani, P. A., Sales, L. V., Pillepich, A., et al. 2016, *MNRAS*, 455, 2323
- Mok, A., Balogh, M. L., McGee, S. L., et al. 2013, *MNRAS*, 431, 1090
- Moster, B. P., Somerville, R. S., Maulbetsch, C., et al. 2010, *ApJ*, 710, 903
- Muzzin, A., Wilson, G., Yee, H. K. C., et al. 2012, *ApJ*, 746, 188
- Naab, T., Johansson, P. H., & Ostriker, J. P. 2009, *ApJL*, 699, L178
- Peng, E. W., Jordán, A., Blakeslee, J. P., et al. 2009, *ApJ*, 703, 42
- Peng, E. W., Jordán, A., Côté, P., et al. 2008, *ApJ*, 681, 197
- Peng, E. W., Ferguson, H. C., Goudfrooij, P., et al. 2011, *ApJ*, 730, 23
- Peng, Y.-j., Lilly, S. J., Kovač, K., et al. 2010, *ApJ*, 721, 193
- Peng, Y.-j., Lilly, S. J., Renzini, A., & Carollo, M. 2012, *ApJ*, 757, 4
- Postman, M., Franx, M., Cross, N. J. G., et al. 2005, *ApJ*, 623, 721
- Postman, M., Lauer, T. R., Donahue, M., et al. 2012, *ApJ*, 756, 159
- Purcell, C. W., Bullock, J. S., & Zentner, A. R. 2007, *ApJ*, 666, 20
- Rhode, K. L. 2012, *AJ*, 144, 154
- Rodriguez-Gomez, V., Pillepich, A., Sales, L. V., et al. 2016, *MNRAS*, 458, 2371
- Rudick, C. S., Mihos, J. C., & McBride, C. 2006, *ApJ*, 648, 936
- Rudick, C. S., Mihos, J. C., & McBride, C. K. 2011, *ApJ*, 732, 48
- Rusli, S. P., Erwin, P., Saglia, R. P., et al. 2013, *AJ*, 146, 160
- Schlafly, E. F., & Finkbeiner, D. P. 2011, *ApJ*, 737, 103
- Schombert, J. M. 1988, *ApJ*, 328, 475
- Seigar, M. S., Graham, A. W., & Jerjen, H. 2007, *MNRAS*, 378, 1575
- Sereno, M., Ettori, S., Umetsu, K., & Baldi, A. 2013, *MNRAS*, 428, 2241
- Sérsic, J. L. 1968, *Atlas de Galaxias Australes* (Cordoba: Observatorio Astronomico)
- Smethurst, R. J., Lintott, C. J., Bamford, S. P., et al. 2017, *MNRAS*, 469, 3670
- Smith, R., Sánchez-Janssen, R., Fellhauer, M., et al. 2013, *MNRAS*, 429, 1066
- Spitler, L. R., & Forbes, D. A. 2009, *MNRAS*, 392, L1
- Spitzer, L., Jr., & Baade, W. 1951, *ApJ*, 113, 413
- Stetson, P. B. 1987, *PASP*, 99, 191
- Tal, T., Dekel, A., Oesch, P., et al. 2014, *ApJ*, 789, 164
- Tanaka, M., Kodama, T., Arimoto, N., et al. 2005, *MNRAS*, 362, 268
- Thomas, J., Ma, C.-P., McConnell, N. J., et al. 2016, *Nature*, 532, 340
- Trujillo, I., Erwin, P., Asensio Ramos, A., & Graham, A. W. 2004, *AJ*, 127, 1917
- van den Bergh, S. 1958, *The Observatory*, 78, 85
- van den Bosch, F. C., Aquino, D., Yang, X., et al. 2008, *MNRAS*, 387, 79
- van der Wel, A., Bell, E. F., Holden, B. P., Skibba, R. A., & Rix, H.-W. 2010, *ApJ*, 714, 1779
- Veale, M., Ma, C.-P., Greene, J. E., et al. 2017a, *MNRAS*, 471, 1428
- Veale, M., Ma, C.-P., Greene, J. E., et al. 2017b, *arXiv:1708.00870*
- Vílchez-Gómez, R. 1999, *The Low Surface Brightness Universe*, 170, 349
- Vulcani, B., Poggianti, B. M., Fasano, G., et al. 2012, *MNRAS*, 420, 1481
- West, M. J., Cote, P., Jones, C., Forman, W., & Marzke, R. O. 1995, *ApJL*, 453, L77
- West, M. J., Côté, P., Marzke, R. O., & Jordán, A. 2004, *Nature*, 427, 31
- West, M. J., Jordán, A., Blakeslee, J. P., et al. 2011, *A&A*, 528, A115
- Wetzell, A. R., Tinker, J. L., Conroy, C., & van den Bosch, F. C. 2013, *MNRAS*, 432, 336
- White, R. E., III 1987, *MNRAS*, 227, 185
- Yahagi, H., & Bekki, K. 2005, *MNRAS*, 364, L86
- Zwicky, F., & Humason, M. L. 1964, *ApJ*, 139, 269